Kufa Journal of Engineering
Vol. 16, No. 4, October 2025, P.P. 87- 124
Article history: Received 28 August 2024, last revised 19 November 2024, accepted 5 December 2024

OPTIMIZING CATALYST PERFORMANCE: A STUDY OF SUPPORT ADDITION EFFECTS ON LA-NI-MN IN CATALYTIC DRY REFORMING OF METHANE

Halah A. Ramadhan[1], and Maha Al-Ali [2]

[1] Department of Chemical Engineering,College of Engineering,Tikrit University, Tikrit, Iraq. Email: halah.a.ramadhan42116@st.tu.edu.iq

[2] Department of Oil and Gas Refining,College of Petroleum Process Engineering, Tikrit University, Tikrit, Iraq. Email: maha.al.ali@tu.edu.iq

https://doi.org/10.30572/2018/KJE/160405

ABSTRACT

In this work, the effect of the support addition to LaNiMnO3 perovskite catalyst is investigated. Perovskite catalysts are prepared via the sol-gel method, namely LaNiMnO3 (LNMO3), LaNiMnO3/MCM-41 (LNMO3/MCM-41), and LaNiMnO3/TiO2 (LNMO3/TiO2). The catalysts are characterized using BET, TGA, XRD, FE-SEM, EDS, and FTIR techniques. The catalytic performances of those catalysts are evaluated in the catalytic dry reforming of methane to produce synthesis gas (H2 and CO). The results of this study indicate that the LNMO3/MCM-41 presents the highest rates of conversion for CH4 and CO2, with 80.56 and 76.32%, respectively. The optimal temperature of reaction to obtain the highest conversion of syngas is 800 °C. The order of activity and stability can be presented as LNMO3/MCM-41> LNMO3/TiO2 >LNMO3. To conclude, this research develops new catalysts with high catalytic performance to improve syngas production from the reaction of methane with carbon dioxide.

KEYWORDS

Methane dry reforming, Lanthanum-Nickel-Based Catalyst, Titanium, MCM-41, Perovskite, Catalyst activity, Hydrogen.

1. INTRODUCTION

The atmospheric system is currently experiencing a major buildup of greenhouse gases (GHGs), which is widely agreed upon to result in severe consequences with regard to climate change. Industrial emissions of flue gases consist of carbon dioxide, nitrogen oxides (NOx), hydrocarbons, carbon monoxide, fine particles, and sulfur dioxide (Rahman et al., 2017, Ali et al., 2024). The energy supply at the current time is mostly derived from fossil fuels, but fossil fuels possess the drawback of rapid depletion and increased greenhouse gas emissions (CH_4 and CO_2) (Ishaq and Dincer, 2021). For decades, there has been enormous global interest in creating processes by which natural gas could be converted to more useful products for the economy's benefit (Daza et al., 2008). The most promising renewable energy carrier for the next few decades is hydrogen (H_2), which is being investigated in numerous technological fields as a promising alternative to fossil fuels (Bahruji et al., 2010). Syngas is produced by a large number of reforming reactions such as dry reforming, partial oxidation, and steam reforming of methane. Catalytic dry reforming of methane (CDRM) is a very effective method in utilization of two greenhouse gases (CH_4 and CO_2) (Cao et al., 2016, Xu et al., 2019) to produce synthesis gas ($CO + H_2$). This method has gained a big interest in recent years since it provides a cost-effective system to convert two low-cost gases into liquid hydrocarbons via the Fischer-Tropsch process (Gallego et al., 2006).

Many researchers used and studied this process at their researches. For instance, (Amin et al., 2013) established that the DRM reaction, which involves the catalytic reaction of methane with carbon dioxide ($CH_{4(g)} + CO_{2(g)} \rightarrow 2CO_{(g)} + 2H_{2(g)}$), they defined it as a possibly effective method for the chemical transformation of CH_4 and CO_2 to syngas (Amin et al., 2013). Also, (Dekkar et al., 2020) showed that converting CO_2 and CH_4 into synthesis gas is a cost-effective and environmentally beneficial procedure; they used a catalyst of Ni/Al_2O_3, which had good catalytic activities in the CDRM reaction both with regard to activity, selectivity, and stability. In which stability under long-term test exceeded 66 hours (Dekkar et al., 2020). The CDRM process is endothermic process; it usually starts at high temperature. Therefore, the decline in starting temperature is crucial to this process. Hence, the use of a good catalyst is expected to work in this regard (Li et al., 2020). Nickel-based catalysts are commonly utilized for catalytic dry reforming of methane (CDRM) due to their high activity and inexpensive cost (Sun et al., 2021), in comparison with noble metal catalysts such as catalysts including Ru, Rh, Pt, and Pd, they have high catalytic activity and strong coke resistance for CDRM reactions, but their high cost and restricted availability limit their industrial applicability. Nickel-based catalysts, particularly supported ones, are widely utilized in reforming reactions (Zhang et al., 2017, de

Araujo et al., 2008). Hence, developing a cost-effective and efficient Ni-based catalyst for CDRM reaction is very desirable. Several efforts have been made to develop strong Ni-based catalysts with uniformly dispersed particles, thus researchers have focused on studying highly stable and active catalysts for CDRM such as noble metal catalysts, transition metal catalysts, supported catalysts, spinel, perovskite, and mesoporous catalysts (Jang et al., 2019). It has been reported that the incorporation of nickel into a structure that is well-defined, such as perovskites, may reduce the rate of deactivation (Sellam et al., 2019). Perovskites which have an ABO_3 structural formula (Abdulrasheed et al., 2019), gained interest in heterogeneous catalysis reactions due to their strong Lewis basicity, which allows for a variety of catalytic processes. Besides their basicity, these oxides have the potential to control ensemble size, thereby minimizing carbon production (Bian et al., 2020, Johansson et al., 2014). There are many kinds of perovskites like ($LaNiO_3$, $BaTiO_3$, $CaSiO_3$, $CaTiO_3$, and $MgSiO_3$). However, the $LaNiO_3$ catalyst is the most commonly used for the CDRM reaction. In addition, $LaNiO_3$ can be modified through the process of partial substitution of the A-site and/or B-site (Chai et al., 2018). $LaNiO_3$ catalyst and its derivatives previously had been recommended as good catalysts for CDRM process due to their structure which have high metal dispersion and a good resistance to carbon formation (Touahra et al., 2016, Pereñiguez et al., 2012). The $LaNiO_3$ perovskite maintains tiny Ni metal particles upon stable support (La_2O_3) that prevents carbon deposition (Goldwasser et al., 2005). In addition, the formed La_2O_3 reacts with CO_2 to form $La_2O_2CO_3$, which aids in avoiding coke formation through the reaction. A lot of researchers established $LaNiO_3$ catalyst, for instance, (Gallego et al., 2006). they prepared $LaNiO_3$ and La_2NiO_4 catalysts by the self-combustion method and they had been applied in the CDRM process. The prepared catalysts proved good catalytic performance in terms of activity and stability as well as good carbon formation resistance. Another work was published by (Batiot-Dupeyrat et al., 2005) they also prepared $LaNiO_3$ perovskite. They showed distinct activity and stability through CDRM reaction, with high coke resistance. This result was appertaining to the presence of Ni^0 and $La_2O_2CO_3$ phases. Supported $LaNiO_3$ perovskite and its derivatives also were established in several studies for example, (Messaoudi et al., 2018) they prepared bulk La_xNiO_y and $La_xNiO_y/MgAl_2O_4$ catalysts by sol-gel and impregnation methods, with the x values of 1 or 2 and the y values of 3 or 4. The $La_xNiO_y/MgAl_2O_4$ catalysts exhibited higher specific surface areas and nickel dispersion. Moreover, it showed an increasing in the catalytic performance in the CDRM process when it compared with bulk La_xNiO_y due to the improved spreading of nickel and the benefit of the basic support. Another research for (Moradi et al., 2013) they synthesized a $LaNiO_3/c$-Al_2O_3 perovskite catalyst and test its activity in the CDRM reaction.

They obtained good results towards the catalytic activity of $LaNiO_3$/c-Al_2O_3 in terms of methane and carbon dioxide conversions, as well as a high nickel dispersion was obtained, in addition, high resistance to carbon deposition during a 75 hr time of reaction.

In this work, $LaNiMnO_3$ ($LNMO_3$), $LaNiMnO_3$/MCM-41 ($LNMO_3$/MCM-41) and $LaNiMnO_3$/TiO_2 ($LNMO_3$/TiO_2) perovskites were prepared and characterized for catalytic CO_2 reforming of methane. The reason behind using these materials is due to their significant properties.

Considering that MCM-41 distinguished by the large surface area to support extensive dispersion of metal (Nisa et al., 2022), excellent mechanical strength, good heat stability, wide PH value stability, and tunable pore diameter and size, which is useful in executing size and shape of specific organic syntheses under hard experimental conditions (Alahmad, 2012). In addition, MCM-41 can improve the catalytic performance of a catalyst by inhibiting SO_2 poisoning (Nguyen et al., 2002)) and due to the presence of mesopores, through which the metal can have an entry into the channels, hence improving the catalytic activity (Singh et al.).

On the other hand, titanium dioxide (TiO_2) is also extensively employed as a catalyst support due to its wide advantages, such as non-toxicity, higher structural stability, low cost, and environmental compatibility. TiO_2 has been applied as a support for metal catalysts in the CDRM process through traditional thermal methods and exhibited perfect coke-resistant property. This improvement is due to the metal-TiO_2 strong interaction that is able to prevent the growth of huge metal particle clusters; it allows for the possibility of increasing active sites for reforming reactions and prevents carbon deposition (Nguyen et al., 2020). This article particularly discusses the activity performance of these catalysts in terms of CH_4 and CO_2 conversions and the stability of these catalysts over time. The study aims to investigate how the addition of (MCM-41 and TiO_2) supports to $LaNiMnO_3$ perovskite catalyst affects its activity and stability under reforming conditions, as well as their characterizations such as the morphology, crystallinity, and surface area.

2. METHODOLOGY

2.1. Materials

Gas of methane was brought from the (Gulf Cryo Company) in Kuwait. Carbon dioxide, nitrogen, and hydrogen gases were purchased from Alnaimi for Gases Company in Baghdad, Iraq, within the specifications and properties of those gases, which are attached in Table 1 below.

Table 1: Properties of the gases utilized in the CDRM experimental runs.

Gas name	Molecular weight (g/mol)	Purity (%)	Density (kg/m³)	Boiling point (°C)	Melting point (°C)	Vapor pressure (psi)	Viscosity (CP)
CH_4	16.04	99.99%	0.656	−161.50	−182.5	913	0.01107
CO_2	44.0095	92%	1.795	−78.464	−78.464	935.5	1.495
N_2	14.0067	98%	1.25	−78.464	−195.8	493	0.01695
H_2	2.016	98%	8.98	−252.87	−259.16	423	0.009

2.1.1. Catalysts active components

Lanthanum nitrate hexahydrate was purchased from Gainland Chemical Company (GCC) with a purity of 99%. Nickel nitrate hexahydrate, Manganese nitrate hydrate, and Citric acid were bought from Sigma Aldrich with a 98% purity. The nitrites were employed in the catalyst preparation as the active materials. Citric acid was used as a co-crystallization emulsifier.

2.1.2. Supports

In this study, two types of supports were used. These materials are nanomaterials which have unique characteristics (Hayal et al., 2021, Abed et al., 2023); MCM-41 (Mobil Composition of Matter), which is a white mesoporous nano-powder having an average pore diameter of 3.4 nm and a pore volume of ≥ 0.75 cm^3/g, with a homogeneous two-dimensional hexagonal structure, and a surface area of around 850 m^2/g. The other support is TiO_2 (titanium dioxide), it is a white nano-powde with 99.9% purity. It has 50 nm average pore size and a 40 m^2/g surface area.

2.2. Method

2.2.1. Catalysts preparation

The sol-gel method reported by Bhavani and Lee by (Bhavani and Lee, 2018) was applied to prepare the unsupported catalyst. This method can ensure a good purity and homogeneity by applying a well-mixing of precursors, which results in a well-partitioned composition. This method also includes modifications of the particle size and surface morphology, results in obtaining a large surface area and high catalytic activity (Navas et al., 2021). The stoichiometric amounts of the used metals: lanthanum nitrate hexahydrate, nickel nitrate hexahydrate, and manganese nitrate hydrate were dissolved in a 50 ml of deionized water. Then 3 grams of citric acid were added to the metals solution to obtain the perovskite oxides phases. After that, the solution was put onto stirring on a temperature of 80 °C until the mixture became a green gel. The 80 °C was carefully chosen to ensure a homogenous green gel in order to prepare a powder with regulated particle size and shape. However, the temperature should not raised higher than this value, because it can lead to a cracking in the resulting gel and producing unstable product due to a rapid evaporation process (Dehghanghadikolaei et al., 2018). Then the resulted gel has inserted into oven for a peroid of 14 hr of time at a temperature of 110 C to provide the

crystalline structure, with this evaporation rate we prepare good catalyst properties. Thus, evaporation must be carried out at a relatively high temperature for a long time to obtain high surface area and pore volume (Navas et al., 2021). After that, a powder was obtained, and hence, it was placed in a tubular furnace to accomplish a calcination process for 5 hr at 800 ℃.

The supported samples $LNMO_3$/MCM-41 and $LNMO_3/TiO_2$ were prepared using the same method and procedure, but after keeping the solution at 80 ℃ for a few minutes, 4 g of MCM-41 or TiO_2 was dissolved in 100 ml deionized water and added to the nitrates solution, and kept on stirring until transforming into a green gel, followed by the same procedure of drying and calcination. Fig. 1 illustrates all the steps of preparation.

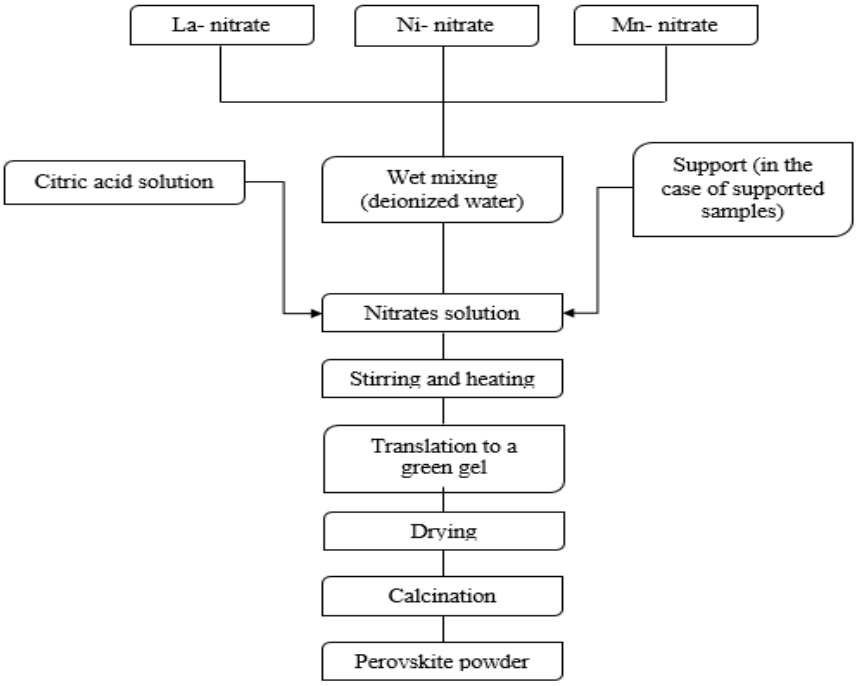

Fig. 1: Schematic diagram for catalysts preparation steps.

2.3. Characterization of the catalyst

X-ray diffraction (XRD), Field emission scanning electron microscope (FE-SEM), and Energy dispersive spectroscopy (EDS) analysis were conducted at Alkhora Nano Lab in Alkhora Company, Baghdad, Iraq. XRD patterns of three samples prepared were measured by Aeris research edition XRD by CuKα radiation on about 1 g of a sample on a specimen holder at room temperature and scanned over a 2θ range of (7.0054 – 79.9904 degrees) using 1.54060 Å wavelength and CuK-α1 radiation at 8 mA and 40 kV. The crystalline structure and morphology of the $LNMO_3$, $LNMO_3$/MCM-41, and $LNMO_3/TiO_2$ samples were characterized through XRD. Field emission scanning electron microscope (FE-SEM) micrograph of the three samples was performed to study the morphology with an Inspect F-50 SEM scanning electron microscope. Catalyst sample samples were studied by placing a small amount of powder sample

on double-sided tabs on Al stubs. After that, vacuum-coating of the powder was carried out at 170 µA and 30 kV. Various images were taken by microscopy. Elemental mapping of our catalysts prepared was found through the analysis of energy dispersive spectroscopy (EDS) based on Axia chemi sem EDS.

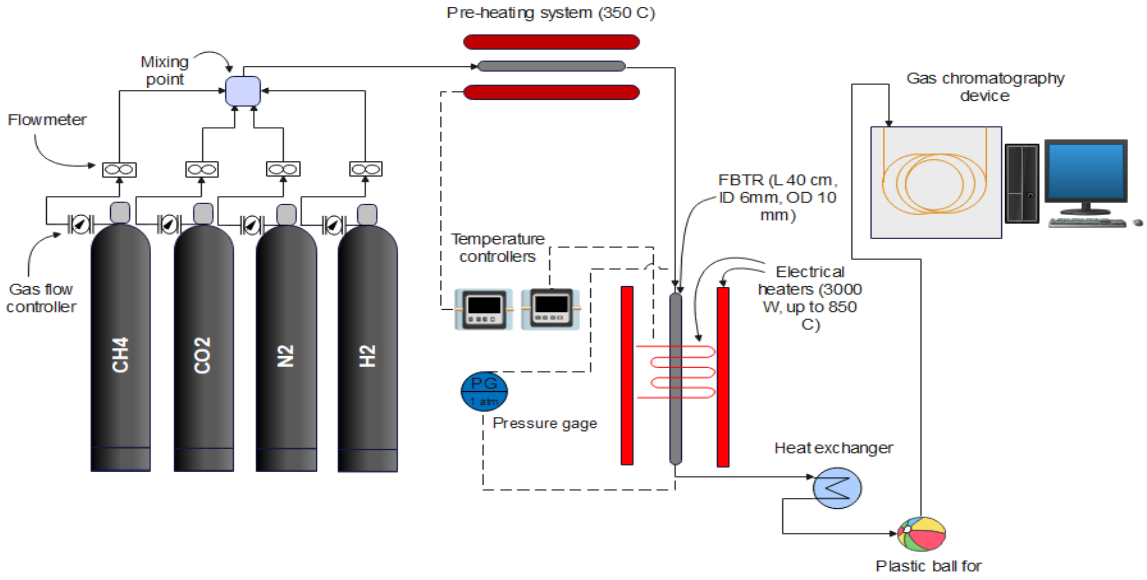

Fig. 2: A block diagram of the catalytic dry reforming of methane process system.

Brunauer-Emmett-Teller (BET) and Thermogravimetric (TGA) tests were carried out at the Petroleum Research and Development Center in Baghdad, Iraq. BET test was applied to determine the specific surface area and the pore size of our three prepared catalysts using the multipoint surface area analysis method. A catalyst sample powder of 0.1 g was positioned in a cell and heated up to 90 °C for one hour, and then the temperature rose to 350 °C for 2 hours. Thermogravimetric analysis (TGA) is a thermal analysis technique that is widely used to examine the thermal properties of a material under thermal conditions (heating process). The test was conducted by raising the temperature from 30 to 800 °C at a temperature ramp equal to 10 °C/min using nitrogen. The sample's mass was recorded during the test period as the temperature continued to rise.

2.4. Reactor set-up

The CDRM reaction was carried out in a fixed bed reactor of specification (height 40 cm, OD 10 mm, ID 6 mm) with a maximum working temperature of 850 °C and heating of 15 °C/min. rate. This type of reactor was chosen because it can provide good interactions between gases and the catalyst's active sites, with flexible regulation of temperature and flow rate (Rase, 2013). Fig. (3.2) shows the reforming system. The reactor consisted of a stainless-steel mesh cup ranging in size from 2 to 5 nm. This mesh cup was used to hold the catalyst powder in the

center of the reactor. The electric heaters of the reactor furnace with 3000 Watt as a capacity that were in a spiral shape surrounded the reactor and shielded with a cylinder of a stainless-steel material. These heaters provide the heat required to accomplish the CDRM reaction (Kim et al., 2023).

2.4.1. Experimental procedure

An amount of about 100 mg of $LNMO_3$ catalyst powder was put in the reactor bed by utilizing a mesh cup centered in the tube. A 50 ml/min hydrogen gas flow was opened for 30 min at a temperature of 800 °C and flowed on the catalyst to activate it before the reaction started. Then methane, carbon dioxide, and nitrogen gases were presented to the reactor tube at a rate of 60 ml/min at a ratio CH_4:CO_2:N_2 of 30:15:15 ml/min and pressure 1 atm. The flow rates of hydrogen and feed gases (N_2:CH_4:CO_2) were sufficient to provide a complete reduction and reaction process, and they were chosen to be suitable for the reactor volume (Li et al., 2021). Gases flowmeters are utilized to control the flow of these gases individually. The initial heating temperature for these gases before entering the reactor was 450 °C to prepare them for reaction under high temperatures and make the reaction faster (Thiers et al., 2000), where the temperature of the reactor furnace was set at four operating temperatures: 500, 600, 700, and 800 °C. The product gas was withdrawn from the reactor bed and assembled by plastic balls equipped with a secure valve, which ensures no air can enter or gas escapes after being filled, in order to be analyzed in the gas chromatograph (GC) device to calculate the conversion rates of methane and carbon dioxide gases. The same steps were re-established, and product samples were withdrawn 1 hour after the reaction to be analyzed. The reactor underwent a second cleaning and was then refilled with the initial catalyst. The activation procedure was thereafter conducted by introducing hydrogen gas. Gases were introduced into the reactor in the same amounts as in step one, maintaining a consistent temperature of 800 °C at an equal duration of time 1, 2, 3, 4, 5, 6, 7, 8, 9, 10, and 15 hours. The data collected were analyzed by calculating the proportion of methane gas remaining after the process and calculating its conversion rates. The process parameters are shown in Table 2.

Table 2. Variable parameters utilized in the process.

Variables	Variables number	Values
Sample	3	$LNMO_3$, $LNMO_3$/MCM-41, $LNMO_3$/TiO_2
Temperature in (ºC)	4	500, 600, 700, and 800
Reaction time in (hour)	15	(1, 2, 3 ~ 15)

3. RESULTS AND DISCUSSION

3.1. Catalyst Characterization

3.1.1. BET results

The values of the specific surface areas of $LNMO_3$, $LNMO_3$/MCM-41 and $LNMO_3/TiO_2$ are 5.87, 156.4 m^2/g, and 21.7 m^2/g, respectively. In addition, the pore volume of these catalysts, respectively, are found to be 0.015, 1.532, and 0.020 cm^3/g. These values proved that the support addition also increases the surface area and pore volume. This increment in surface area and pore volume provides more active sites and increases the catalyst surface capacity for the reactants, hence improving the catalyst activity (Wang et al., 2013).

$LNMO_3$ has a very low surface area, which can be attributed to the high calcination temperature (Khalesi et al., 2008). However, a high surface area is obtained for $LNMO_3$/MCM-41 (156.4 m^2/g) compared to $LNMO_3$ (5.87 m^2/g). In contrast, $LNMO_3/TiO_2$ sample showed a moderately high value of surface area about (21.4 m^2/g) higher than $LNMO_3$ sample. Comparable results were attained by many studies. The catalysts surface area has increased after supports addition, consequently improved performance and properties were noticed due to the increment in active sites number and metals dispersion, which is can be related to the porous structures of the supports (Wang et al., 2013). Another study accomplished by (Makshina et al., 2006) they prepared $LaCoO_3$ and $LaCoO_3$ catalysts supported on mesoporous (MCM-41). They showed higher values of surface area and catalytic conversions after the perovskites incorporation on the MCM-41 support (Makshina et al., 2006). As well as, (Duan et al., 2017) synthesized bulk $LaNiO_3$ and supported $LaNiO_3$ over SBA-15 catalysts. They showed that the catalyst with support had an improved surface area and higher metal dispersion in which Ni particles are uniformly distributed over the support matrix, and more Ni sites improved the catalyst catalytic performance (Duan et al., 2017). Another significant study was conducted by (Yadav and Das, 2019), while conducting their research they prepared a number of bulk and supported $LaNi_xFe_{1-x}O_3$ perovskites supported over different supports: Al_2O_3, SiO_2, and MgO. They proved that the incorporation of support improved the dispersion of the perovskite phase in which the perovskite $LaNi_xFe_{1-x}O_3$ was dispersed in the pores of the support material and improved the surface area and pore volume of bulk perovskite. The larger surface area benefits in inhibiting sintering of the Ni nanoparticles, results in activity improvement (Yadav and Das, 2019). (Zhang et al., 2014) in their research they prepared a series of LaMn-based perovskite catalysts and; TiO_2 and CeO_2 supported LaMn-based perovskites. Their BET test showed an increase in the surface area after adding the support owing to the high surface areas of (TiO_2 and CeO_2) and the dispersion of the perovskites over the supports, as well as the support addition modified the catalytic performance through enhancing the redox capacity and altering the nitrites/nitrates cumulant (Zhang et al., 2014).

3.1.2. TGA analysis

The weight loss of the perovskite catalysts was measured by TGA analysis. Figs. 3 (a, b, and c) shows the TGA trends of the three prepared catalysts. The curve can be divided into four stages from Fig. 3a, which indicates the unsupported $LNMO_3$ catalyst. A) a rapid weight decrease below 150 ℃ due to the water evaporation (Ma et al., 2021); B) a slight weight increase from 150 ℃ to 400 ℃ because of the oxidation of the metallic species: lanthanum, nickel, and manganese, to oxides, which is in consensus with the study of (Shahnazi and Firoozi, 2021, Gallego et al., 2009); C). Then, the curve rapidly decreases in the temperature range (400 ℃ to 600 ℃) due to the decomposition of carbon deposits ($C + O_2 \rightarrow CO_2$), which is in agreement with (Liu et al., 2020, Yang et al., 2015). Finally, Finally, D) the curve is slightly raised after 600 ℃, related to a weight gain due to the $La_2O_2CO_3$ compound formation (Komarala et al., 2019).

The obtained curve for the $LNMO_3$/MCM-41 catalyst, as shown in Fig. 3b could be divided into three stages. A) a rapid weight loss below 150 ℃, due to extensive moisture release The obtained curve for the $LNMO_3$/MCM-41 catalyst, as shown in Fig. 3b, can be divided into three stages. A) a rapid weight decrease below 150 ℃, due to extensive moisture release (Amin et al., 2013); B) the curve increases slightly in the range between 150 ℃ and 250 ℃, representing a gain in weight for this catalyst, which could be attributed to the oxidation of metal species (Zhao et al., 2016); C) after 250 ℃ a weight loss is addicted which corresponds to the carbonaceous residues reduction in the perovskite structure (Li et al., 2018); and the catalyst weight steadily decreases up to 800 ℃.

The curve may be divided into five stages, as shown in Fig. 3c, which shows the $LNMO_3/TiO_2$ catalyst. A) the weight loss due to moisture release (Amin et al., 2013); then B) a weight gain above 120 ℃, which is due to the oxidation of metallic species (Zhao et al., 2016); C) after 260 ℃ a weight loss is detected related to the thermal decomposition of tightly coordinated carbon source such as carbonates (Yang and Moon, 2016); D) there is a weight gain in the temperature range of (350-600 ℃) which is related to the reduction of NiO nanoparticles supported on TiO_2 (Yang and Moon, 2016); and E) above 650 ℃ a weight loss is observed which is related to the combustion of graphite carbon (Zhao et al., 2016). As a result, the addition of TiO_2 material as a support to the $LNMO_3$ perovskite decreases the weight loss or carbon deposition hence the weight loss of $LNMO_3$ and $LNMO_3/TiO_2$ is 1.34% and 0.93%, respectively, but the weight loss in the case of MCM-41 is 2.91%.

A same result using $LaNiMnO_3$ as a catalyst in their research was reported by (Komarala et al., 2019) for their prepared catalyst $LaNi_{0.8}Mn_{0.2}O_3$ that they synthesized. The catalyst showed a

mass gain of around 6% corresponding to lanthanum oxycarbonate ($La_2O_2CO_3$) that formed due to the reaction La_2O_3 with CO_2 (Komarala et al., 2019). Another work reported by (Rabelo-Neto et al., 2018) indicated by their research that the supporting $LaNiO_3$ on Al_2O_3 decreased the carbon deposition around 1/3 of the unsupported $LaNiO_3$ catalyst, and the supported $LaNiO_3$ over $CeSiO_2$ eliminated the carbon formation practically, due to the higher amount oxygen storage capacity of $CeSiO_2$. They indicate that the role of support is very important in minimizing the amount of carbon deposits formation since the mechanism of CDRM reaction is a dual path. The first path is the methane dissociation, resulting in hydrogen and active carbon species, and the other path is carbon reaction with oxygen from the Al_2O_3 support. Thus, the catalyst surface is kept clear of carbon deposits (Rabelo-Neto et al., 2018).

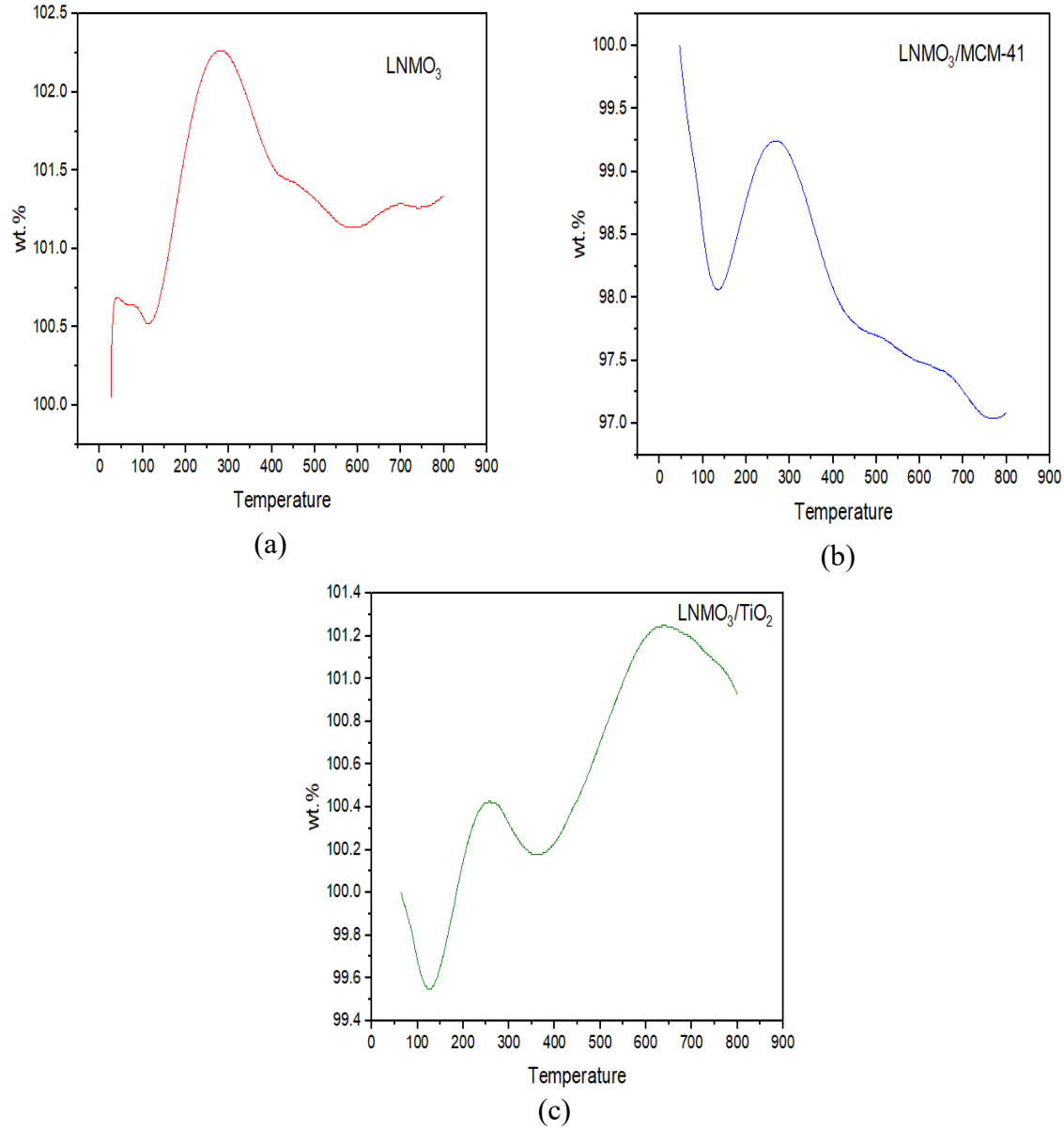

Fig. 3. TGA analysis images of (a) $LNMO_3$, (b) $LNMO_3$/MCM-41, and (c) $LNMO_3/TiO_2$ samples.

3.1.3. XRD results

The internal structure of our three prepared samples were characterized by using X-ray Diffraction. XRD analyses was carried out to characterize the internal structure of the synthesized catalysts (Moradi and Rahmanzadeh, 2012). Figs. 4 (a,b,c and d) represent the XRD patterns of $LNMO_3$, $LNMO_3$/MCM-41, and $LNMO_3/TiO_2$. Fig. 4a shows that the diffraction lines are exactly at 2θ° =22.9°, 32.7°, 37.3°, 40.2°, 43.2°, 46.9°, 52.7°, 58.2°, 62.8°, 68.4°, 73.0°, 75.3°, 78.2° and 79.5°. From these obtained values, the asymmetric peak at 2θ°=22.9° indicates the formation of rhombohedral perovskite structure $LaNiO_3$ with high crystallinity (Gallego et al., 2006, Komarala et al., 2019), and the sharp peak at 2θ°=32.7° demonstrate the formation of a solid solution of La-Ni-Mn-O (Valderrama et al., 2018). As well as the peaks at 43.2°, 75.5°, and 52.8° correspond to the NiO compound (Sharma et al., 2019), and the small weak peaks corresponded to the MnO phase (Shahnazi and Firoozi, 2021). Additionally, the peak at 2θ°=58.2° can be related to the reflection plan of the $LaMnO_{3.15}$ phase, rhombohedral, non-stoichiometric excess oxygen $LaMnO_{3+\delta}$ (Zhu et al., 2010). Fig. 4b represents the catalyst after the addition of MCM-41 support. from the figure, the XRD peaks are at 2θ°= 23.3°, 28.6°, 30.7°, 37.5°, 43.6°, 63.1°, 75.7° and 79.7°. It is observed that the peaks are weaker than those for the unsupported sample. This can be attributed to the fact that MCM-41 channels' have asymmetrical arrangement (Han et al., 2018). The broad peak seen in the XRD patterns at around 23.3° is attributed to the amorphous silica phase found in the MCM-41 support (Ibrahim et al., 2015). The asymmetric diffraction peak at 2θ°=22.9° is shifted to 28.6°, revealing the rhombohedral perovskite structure $LaNiO_3$ which is still observed even after the MCM-41 addition (Sellam et al., 2019). As well as, the diffraction peak at 2θ°=32.7° is shifted to 37.5° which suggests the generation of La-Ni-Mn-O as a solid solution . Additionaly, the peak at 43.2 is shifted to 43.6, which represents the NiO compound (Valderrama et al., 2018).

For the third sample $LNMO_3/TiO_2$, Fig. 4c, the diffraction peaks are found at 2θ°=23.9°, 25.1°, 32.7°, 35.4°, 37.6°, 40.6°, 47.9°, 49.1°, 53.7°, 55.0°, 62.7°, 63.7°, 68.6°, 70.1° and 75.0°. The perovskite structure is also showed for the catalyst with TiO_2 support at 2θ°=22.9° but it is shifted to 23.9° which points to the $LaNiO_3$ phase, and the diffraction peak at 2θ°=32.7° is shifted to 25.1° which indicates the formation of La-Ni-Mn-O solid solution, while the peak at 2θ°= 37.6° is related to the TiO_2 material (Nuvula et al., 2018, Kim et al., 2012). Regarding the other two samples, the NiO compound is also observed at 49.1 degrees. In the support addition situation, the $LaMnO_{3.15}$ phase has approximately disappeared, which can be represented to the fact that perovskite dilution happened due to the support addition (Zhang et al., 2014). In the all samples, no impurities such as $NiMnO_3$ or $Ni_3Mn_2O_8$ were showed (Bhavani et al., 2013),

and La_2O_3 (Sagar et al., 2014), metallic Nickel (Frontera et al., 2013, Zhang and Liu, 2020) were detected at (2θ°=28.6°, 46.9° and 55.0°) and at 44.6°, respectively. NiO is the main phase for all samples, which resulted from Ni oxidation as-prepared catalyst (Özbay and Şahin, 2017). These observations tell us that the support addition does not affect the essential components of $LNMO_3$ perovskite.

Comparable results to our $LNMO_3$ catalyst obtained by several researchers in which their catalysts showed similar patterns and structures as we obtained for our catalyst. For example, (Blasco et al., 2002) synthesized $LaNi_{1-x}Mn_xO_{3+\delta}$ in which x is equal to 0.1, 0.25, 0.5, 0.75, and 0.9 by the sol-gel preparation method. The XRD test indicates for the crystallographic structure an orthorhombic $LaMnO_3$ phase in the catalyst region that is rich with Mn and rhombohedral $LaNiO_3$ structures in the catalyst region that is rich with Ni for $LaNi_{0.5}Mn_{0.5}O_{3+\delta}$. Their test also showed diffraction peaks that indicated the presence of Ni and Mn atoms (Blasco et al., 2002). Another study was reported by (Hou et al., 2014), who synthesized $LaMn_{1-y}Ni_yO_3$ in which (y =0.1, 0.25, and 0.4) perovskite catalysts. They gained XRD patterns for an orthorhombic $LaMnO_3$ phase and rhombohedral $LaNiO_3$ phase for all catalysts and a diffraction peak for NiO at 2θ equal to 43.3 (Hou et al., 2014). Another study by (Zhang et al., 2020) prepared a study for $LaMn_{1-x}Ni_xO_3$ in which (x = 0, 0.1, 0.2, and 0.3) catalysts. They indicated that the Ni-substituted $LaMnO_3$ catalysts showed perovskite characteristics and a diffraction peak for $LaMnO_{3.15}$ (Zhang et al., 2020), and the same phase was showed with our catalysts. In addition, (Dinamarca et al., 2016) prepared a perovskite catalyst $LaMn_{0.5}Ni_{0.5}O_3$, and made the XRD characterization test and the results showed a rhombohedral–hexagonal $LaNiO_3$ structure at (2θ°=32.6°) (Dinamarca et al., 2016).

For our supported catalysts, similar XRD patterns were reported by (Xu et al.). In their study they prepared $LaNiO_3$/MCM-41 perovskite catalyst. They also obtained lower diffraction peaks, and the XRD test showed peaks for highly ordered hexagonal MCM-41 and $LaNiO_3$, as well as a diffraction peak for LaNi-MCM-41 compound (Xu et al.). Another interesting study reported by (Kira et al., 2007) in which they prepared $LaMnO_3$ nanocrystal catalyst supported on MCM-41. They represented the XRD patterns of the $LaMnO_3$/MCM-41 catalyst and the patterns showed a formation of a rhombohedral phase and a broad diffraction peak for the MCM-41 nanomaterial (Kira et al., 2007). Moreover, (Chen et al., 2020) prepared $LaNiO_3/TiO_2$ catalyst and tested its structural phases by X-ray diffraction (XRD). The test represented several peaks for TiO_2 and $LaNiO_3$ that matches with the standard peaks, as well as there was a reflection for NiO compounds, the same results we obtained with our samples (Chen et al., 2020). A noteworthy study by (Giroir-Fendler et al., 2016), the researchers were synthesized

$LaMnO_3$ catalyst supported on TiO_2 and detected the formation of the $LaMnO_3$ phase on TiO_2 which is used as a support by XRD test. The test confirmed the successful formation of $LaMnO_3/TiO_2$, in which crystallographic structure represented the support is kept while allowing for the growth of $LaMnO_3$ perovskite structure (Giroir-Fendler et al., 2016).

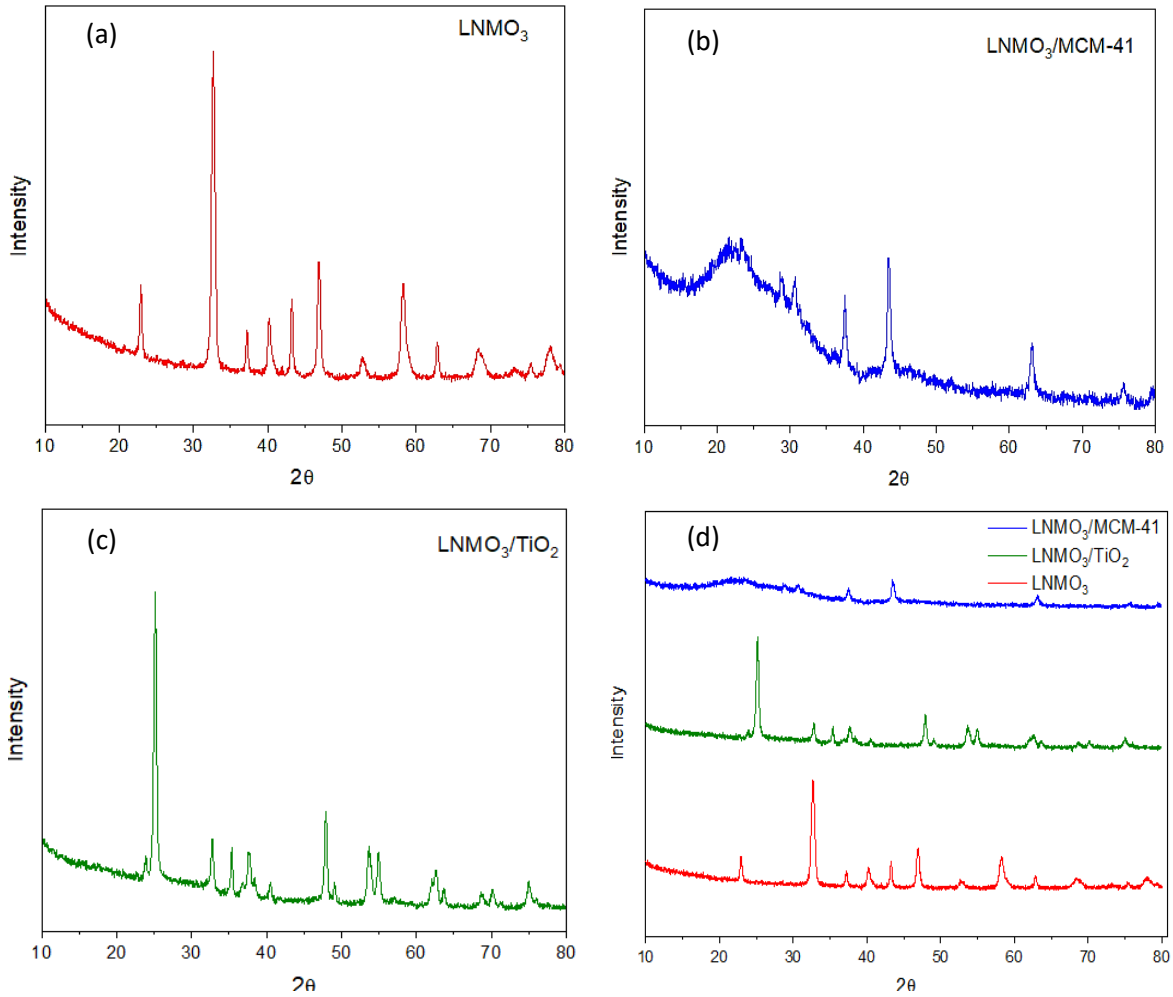

Fig. 4. XRD patterns of (a) $LNMO_3$, (b) $LNMO_3$/MCM-41, (c) $LNMO_3/TiO_2$ samples, and (d) all samples.

3.1.4. FE-SEM results

Field Emission Scanning Electron Microscopy (FE-SEM) examined the prepared catalysts' morphologies. For the $LNMO_3$ sample, the graph in the micro-scale Fig. 5a shows that the particles have irregular shapes. Some of them are larger than others, which agglomerated together to form a more regular shape that looks like cotton with an average particle size of 58.96 nm. After support addition in the case of $LNMO_3$/MCM-41, from Figs. 5c, d, we can observe that the particles tend to take more regular shapes, in which the semi-rod-like particles are aggregated to form larger particles with an average pore diameter of 61.73 nm, which clustered together in the shape of a coral-reef structure. While for the $LNMO_3/TiO_2$ sample, Figs. 5e, f, we can observe the small pseudo-spherical particles bonded together to attain a

regular shape that looks like flakes. This sample has a more uniform shape than the $LNMO_3$/MCM-41, in which the small spherical particles are distributed uniformly. In the two cases, the average particle size increases after the support addition, from 58.96 nm to 61.73 nm and 68.21 nm, respectively. The supported catalysts exhibited better morphology because the nanomaterials (MCM-41 and TiO_2) have the properties of uniform particle sizes and an ability to obtain a better dispersion for the active components as well as prevent the agglomeration of metal particles on their surface and hence the shape becomes more uniform than the unsupported one (Bhattacharyya et al., 2006, Mulewa et al., 2017). Analogous morphologies were obtained by some researchers, for example, (Komarala et al., 2019). They synthesized $LaNi_{0.8}Mn_{0.2}O_3$ catalyst and applied it to the methane reforming reaction. Surface morphology was illustrated by SEM test and the test showed that the perovskite had spherical morphology similar to the shape of our sample ($LNMO_3$). The morphology in this paper is attributed to the presence of $LaNiO_3$, $LaMnO_3$, NiO, and La_2O_3 compounds in the structure of the catalyst (Komarala et al., 2019). A study for (da Silva and Zanoteli, 2020) demonstrated the synthesis of Ni/MCM-41 catalyst and they applied it in DRM reaction. They tested its surface morphology using the SEM test method. The SEM result was identical with $LNMO_3$/MCM-41 catalyst in which support is dominant phase in the determination of catalyst morphology because there is interaction between support and metal and the resulting product catalyst resists the form and pore type of the support (da Silva and Zanoteli, 2020). Another comparative research was conducted (Liu et al., 2020), where they synthesized $LaNiO_3$/MCM-41 catalyst. They were having a similar morphology to our synthesized catalyst (Liu et al., 2020). For the $LNMO_3/TiO_2$ catalyst, the same was also observed by (Baamran and Tahir, 2019), who prepared a Ni/TiO_2 catalyst and tested its morphology. They had particles with semi-spherical shapes and uniform sized particles due to the nature of the crystalline structure of TiO_2, and its stability gives it a uniform particle size (Baamran and Tahir, 2019).

3.1.5. EDS results

The energy dispersive X-ray spectroscopic (EDS) elemental mapping for the three prepared samples $LNMO_3$, $LNMO_3$/MCM-41, and $LNMO_3/TiO_2$ perovskites catalysts are shown in Figs. (6a, b), (7a, b), and (8a, b). The figures show a homogenous allocation of the elements over the surfaces of samples. The peaks belong to the lanthanum, nickel, manganese, oxygen, silicon, and titanium according to EDS spectra. The elements were with the same experimental percentages they were prepared with, and they are dispersed uniformly as they are homogeneously distributed (Liu et al., 2015). These figures prove the formation of $LaNiO_3$ perovskite structures (Wang et al., 2013).

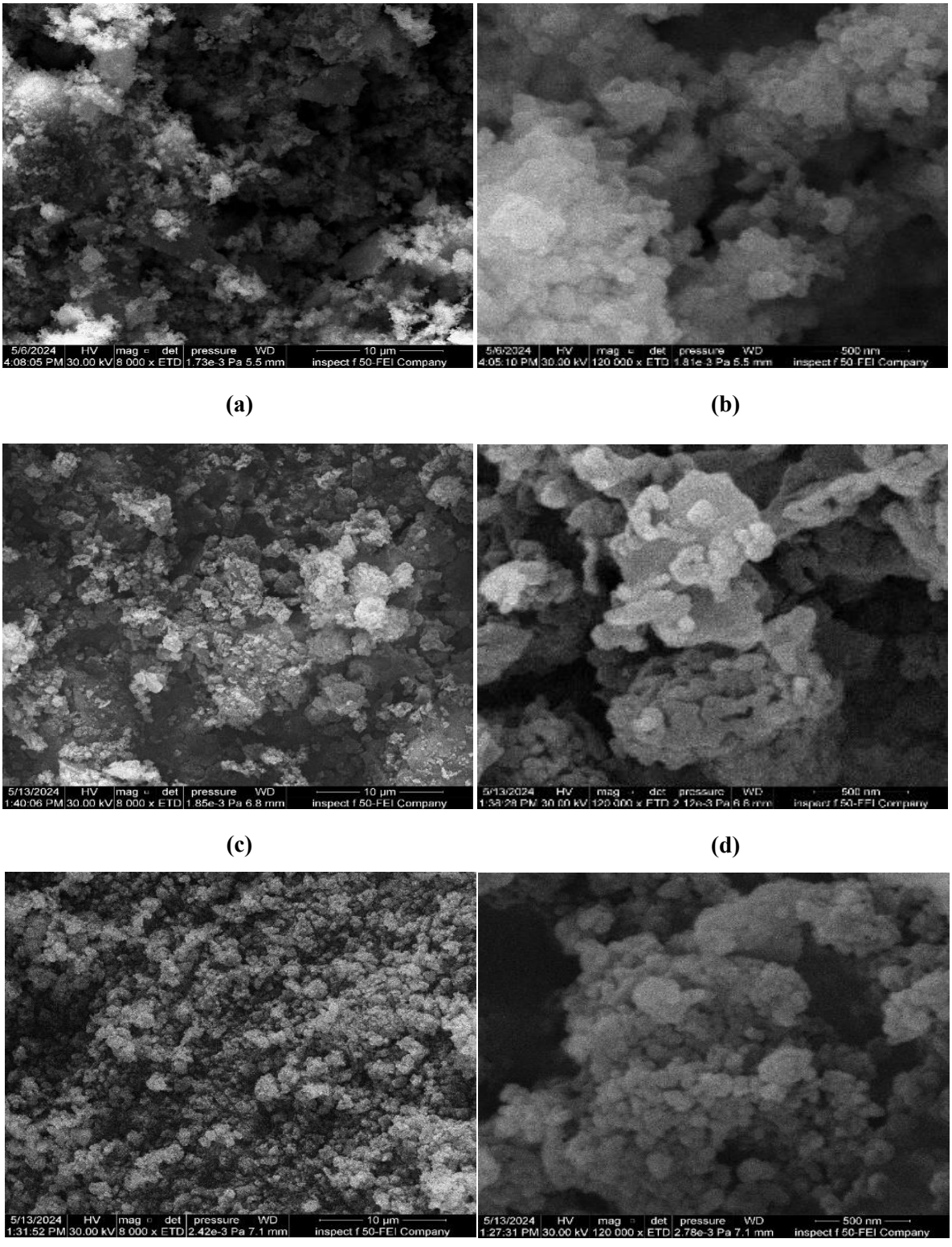

(a) **(b)**

(c) **(d)**

(e) **(f)**

Fig. 5. FE-SEM Images of the catalysts (a), (c), and (e) represent $LNMO_3$, $LNMO_3$/MCM-41, and $LNMO_3/TiO_2$ respectively, in the micro-scale and (b), (d) and (f) represent $LNMO_3$, $LNMO_3$/MCM-41 and $LNMO_3/TiO_2$ respectively, in the nano-scale.

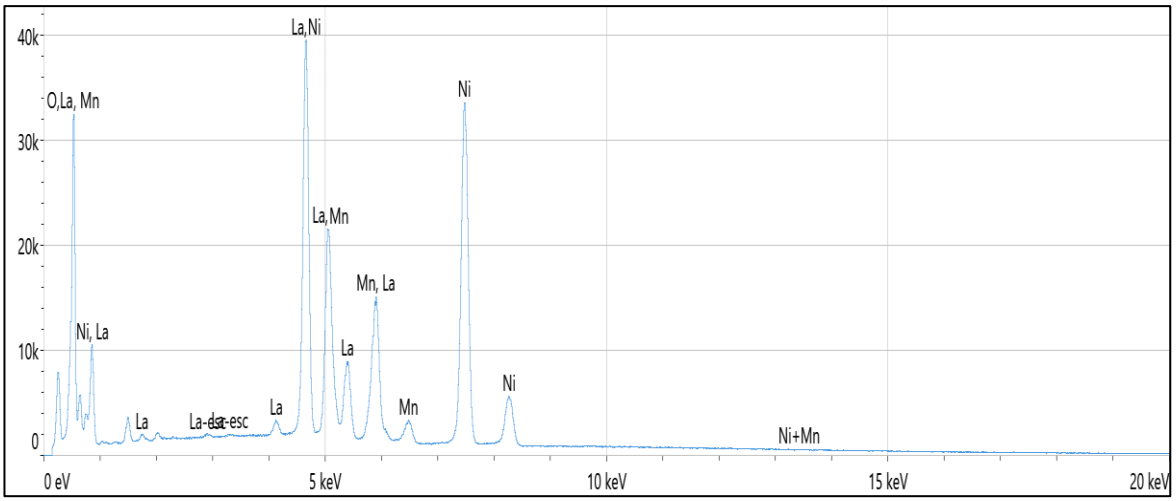

(a)

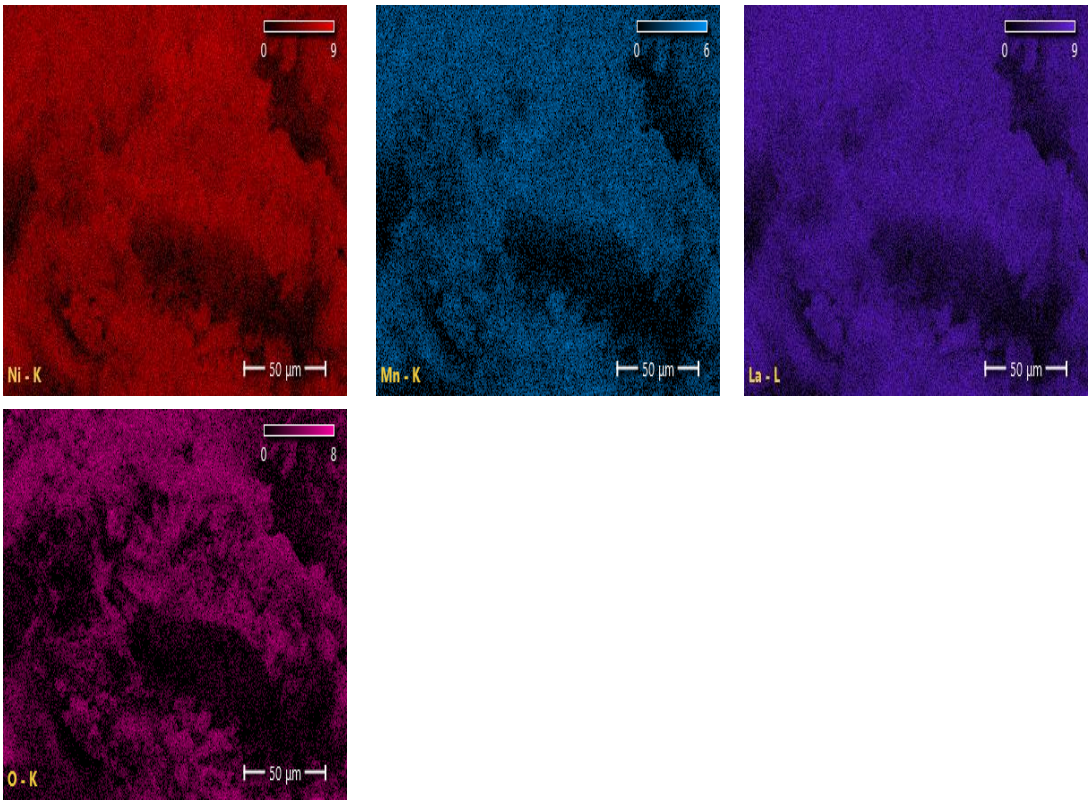

(c)

Fig. 6. (a) EDS map spectrum, and (b) maps of elements distribution, for the LNMO3 sample.

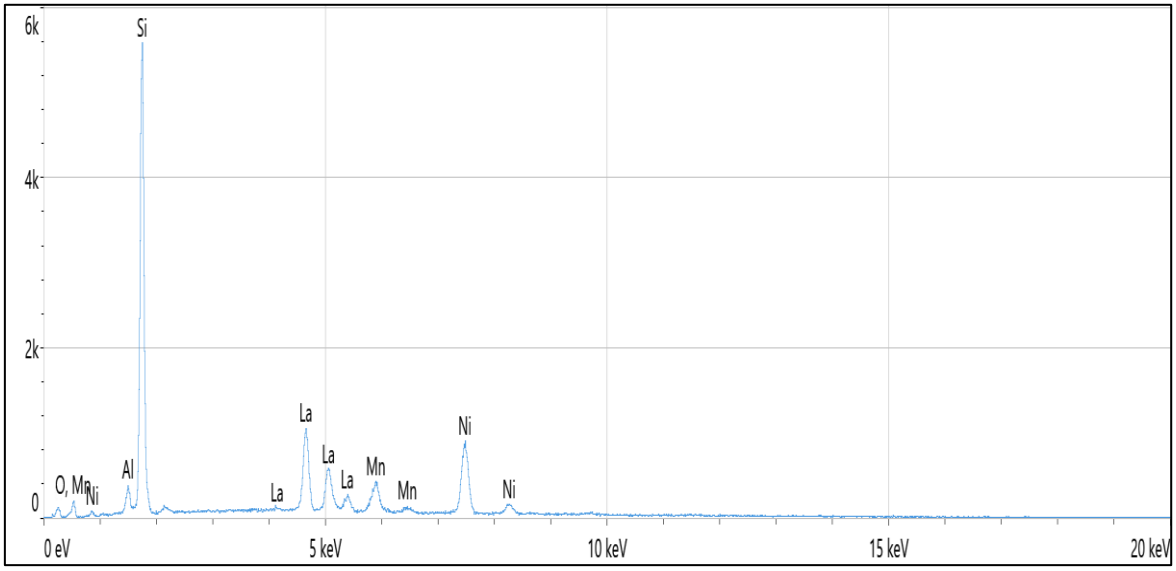

(a)

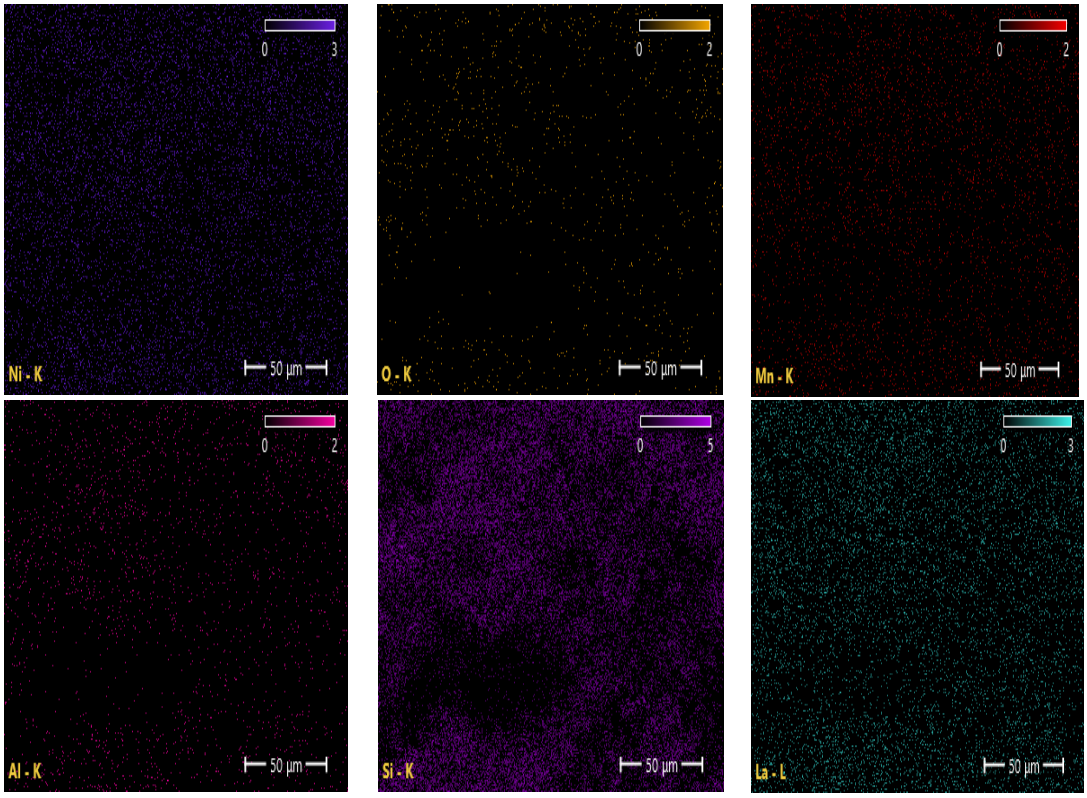

(c)

Fig. 7. (a) EDS map spectrum, and (b) maps of elements distribution, for the $LNMO_3$/MCM-41 sample.

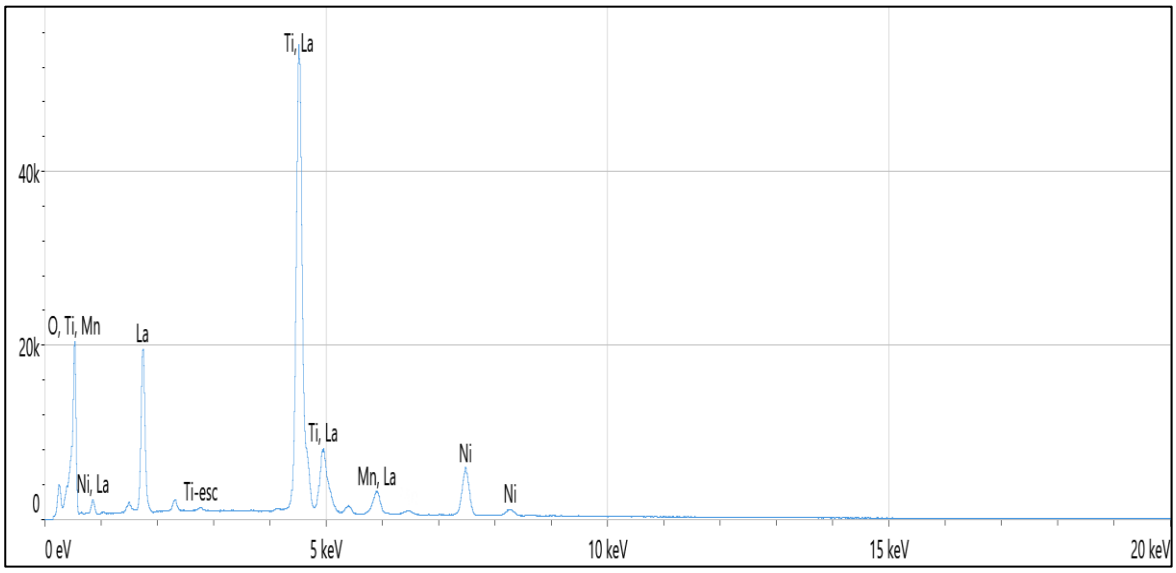

(a)

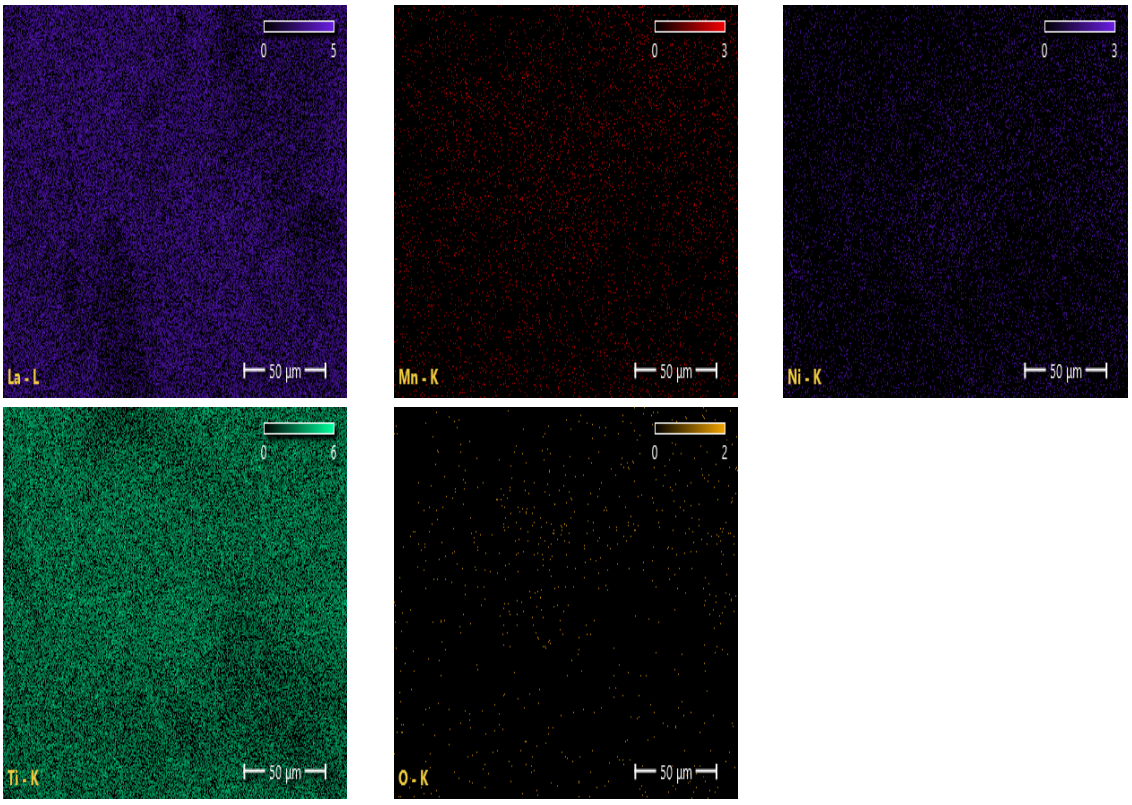

(b)

Fig. 8. (a) EDS map spectrum, and (b) maps of elements distribution, for $LNMO_3/TiO_2$ sample.

3.1.6. FTIR results

Fourier transform infrared spectroscopy (FTIR) is an efficient method for assessing surface chemical species (Hambali et al., 2020). Figs. 9(a, b, and c) represents the FTIR spectra of the calcined $LNMO_3$, $LNMO_3$/MCM-41, and $LNMO_3/TiO_2$ samples in the stretch of 400-4000 cm^-

[1]. For $LNMO_3$, Fig. 9a shows a number of absorption bands at 3456.2, 3188.11, 2925.81, 2746.44, 1961.47, 1647.10, 1089.71, 943.13, 881.41, 744.47 and 597.89 cm^{-1}. The figure shows the peak at 3456.20 $cm^{-1,}$ which is attributed to the combination of the N-H bending mode (Socrates, 2004). A weak band appears at 2925.81 $cm^{-1,}$ representing the hydroxyl (O-H stretch) from the citric acid. Citric acid also possesses stretching vibration of the C=O band in the carboxylic group (-COOH) (Yang and Moon, 2016) and weak bands at 2746.44–1961.47 cm^{-1} related to the Aldehydes (C–H stretch). The band at 597.89 cm^{-1} is related to the Mn-O bond (Zheng et al., 2012). For all samples, the bands (strong bands) at less than 700 cm^{-1} correspond to (M= La, Ni, Mn)–O bond (Vaz and Salker, 2007). All perovskite samples exhibited an adsorption band at around 600 cm^{-1}. This band relates to Mn-O stretching (Hou et al., 2014, Zheng et al., 2012).

After the support addition for the sample $LNMO_3$/MCM-41, Fig. 9b presents a number of absorption bands at 3529.49, 3247.90, 2970.17, 2389.64, 1643.24, 1564.16, 1506.30, 1392.51, 1099.35, 922.63, 669.25 and 491.81. The figure illustrates that in the spectrum of $LNMO_3$/MCM-41, the peak at 3529.49 cm^{-1} is also attributed to the combination of N-H bending mode as for the unsupported sample (Socrates, 2004). The weak band appears at 2970.17 $cm^{-1,}$ representing the hydroxyl (O-H stretch) from the citric acid. The band at 669.25 is attributed to Ni-O stretch, which Ni-O bending results in the perovskite structure (Maridevaru et al., 2020). The band at 929.63 is related to nitrate anions (Omari et al., 2017), and the band at 922.63 is related to Si-OH from MCM-41 material (Farhadi and Mahmoudi, 2019).

$LNMO_3/TiO_2$ sample shows a number of absorption bands at 3506.35, 2970.17, 2393.50, 1647.1, 1558.38, 1238.21, 1058.85, 806.19, 744.47, 466.74 and 460.96, as shown in Fig. 9c. The spectrum of $LNMO_3/TiO_2$ suggests that the peak at 3506.35 cm^{-1} is attributed to the N-H bending mode (Socrates, 2004). The weak band appearing at 2970.17 cm^{-1} represents the hydroxyl (O-H stretch) from the citric acid. The band at 466.74 is representing to the Ni-O bond (Omari et al., 2017).

Comparable result is reported by (Xu et al.), they synthesized $LaNiO_3$/MCM-41 perovskite catalyst and characterized it using infrared spectroscopy test to identify the composite pattern. Their results showed the presence of MCM-41 peak below 1400 cm^{-1} band which is related to the silica material obtained in the MCM-41, and the band at 968 cm^{-1} was associated with (Si-OH) as well as bands at 450 cm^{-1} was related to the band (Si-O-Si), and the same peak was obtained with our catalyst (Xu et al.).

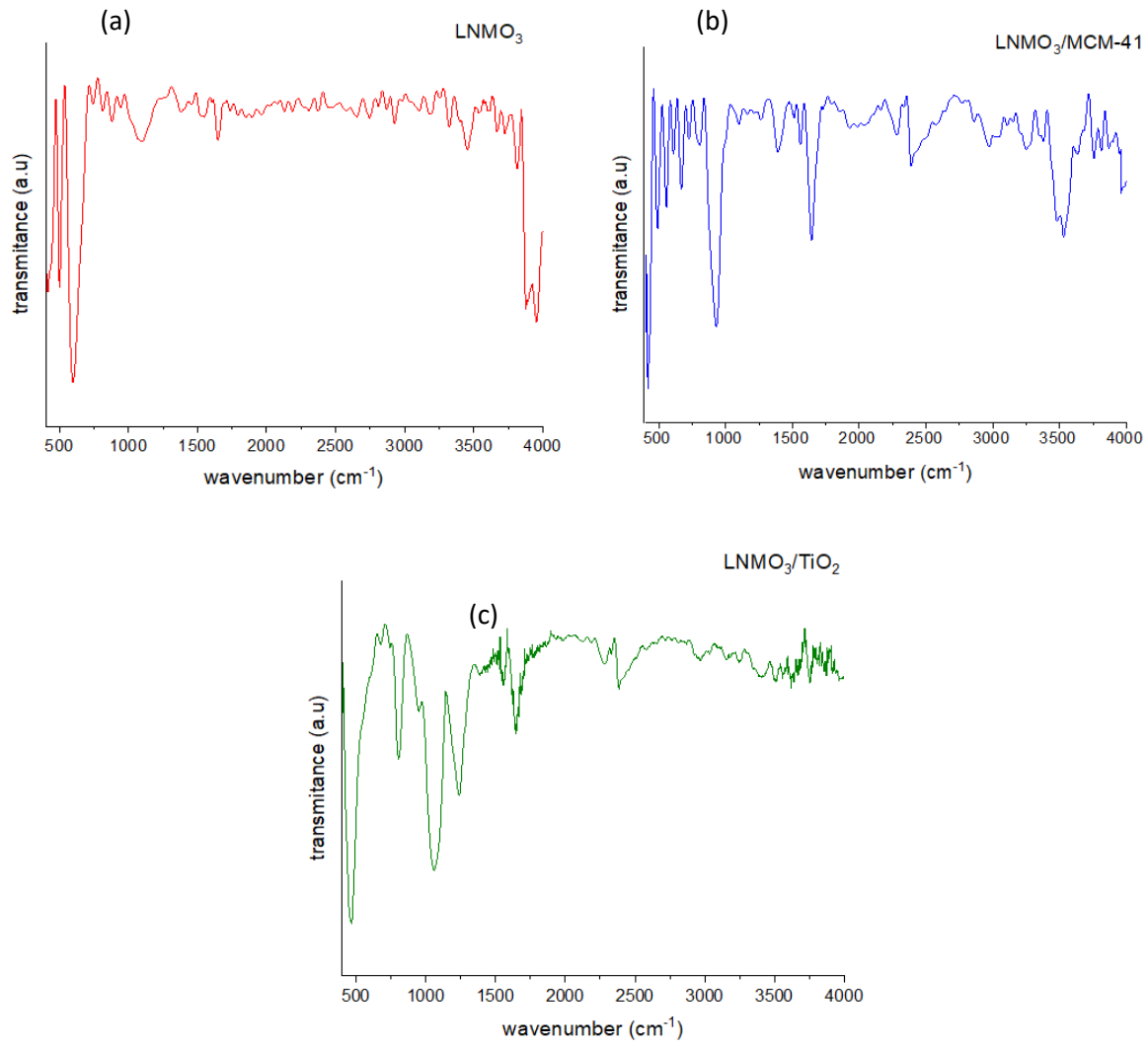

Fig. 9. FT-IR spectrum of (a) $LNMO_3$, (b) $LNMO_3$/MCM-41, (c) and $LNMO_3/TiO_2$.

3.1.7. Temperature effect

The catalyst's efficiency and ability to convert CH_4 and CO_2 to syngas were investigated at various temperatures during continuous time intervals. These temperatures are (500, 600, 700, and 800) °C. This section demonstrates the impact of temperature on reaction conversion rates using $LNMO_3$, $LNMO_3$/MCM-41, and $LNMO_3/TiO_2$ catalysts.

The variations in conversion rates of CH_4 and CO_2 with temperature rising in the CDRM reaction within 1 hr are shown in Figs. 10 (a, b, and c). The conversions of CH_4 and CO_2 for the $LNMO_3$ sample at 500 °C the conversions of CH_4 and CO_2 are 17.26 and 13.71%, respectively. After increasing the temperature to 600, 700, and 800 °C, the conversions become 29.65 and 25.96%, 48.19 and 44.49%, and 67.43 and 62.2% for CH_4 and CO_2, respectively. As a result, the conversions of CH_4 and CO_2 increase with the increase in reaction temperature. This can be attributed to the fact that the CDRM reaction is endothermic. Thus, high

temperatures are required to be effectively performed since the kinetic of dry reforming reaction indicates the need for high temperature to accomplish the main reaction step of methane dissociation and carbon combustion via adsorbed CO_2. As a result, high reaction temperature is an effective parameter (Usman et al., 2015). Fig. 10b displays the result of the experiments of $LNMO_3$/MCM-41, conducted after 1 hr. CH_4 and CO_2 at 500 °C conversion percentages are 21.2 and 17.43%, respectively. These percentages are boosted to 37.56 and 32.8% at 600 °C and then increased to 67.28 and 60.58% at 700 °C for CH_4 and CO_2, respectively. While at the highest conversion was obtained at 800 °C, with 80.56% for CH_4 and 76.32% for CO_2. The third sample, $LNMO_3/TiO_2$, gives opposite conversion results at 500 °C since the CO_2 conversion was higher than the CH_4 conversion due to the reverse water-gas shift reaction (Rabelo-Neto et al., 2018), estimated by 15.74 and 20.58 %, respectively. These percentages increase to 29.9 and 32.87 % for CH_4 and 60.32 and 65.85% for CO_2 when the temperature increases to 600 and 700 °C, respectively. After increasing the reaction temperature to 800 ºC after 1 hour of reaction, the conversions of CH_4 and CO_2 reached a maximum of 68.6 and 70.1%, respectively. As a result, the gas conversions increase after the MCM-41 and TiO_2 addition. This can be attributed to the increment in the number of active sites, thus allowing more reactants to react on the catalyst surface, producing a higher amount of product gas, and due to the strong metal-support interaction, which can prevent the deactivation process at high temperatures (Cargnello et al., 2013).

It was discovered that the optimal reaction temperature for the reaction, ranges from 700 to 800 °C, with 800 °C being the best temperature according to the high rate of reaction conversion. This observation corresponds with the results achieved from the investigation of (Kim et al., 2012). They also used TiO_2 as a support for their catalyst. They prepared a Ni/TiO_2 catalyst and examined its catalytic activity in the CDRM reaction, and they got the highest conversions at 800 °C, 56% CH_4, and 65% CO_2 after 1 hr of reduction treatment (Kim et al., 2012). Another interesting study used MCM-41 as a support in their catalyst, was reported by (Frontera et al., 2013). They prepared Ni catalyst supported on highly ordered silicalite-1 (H-S) and highly defective pure silica MCM-41. The performance tests showed that Ni/MCM-41 provided higher CH_4 and CO_2 conversions at 700 °C (Frontera et al., 2013). A study reported by (Nguyen et al., 2020) in which they prepared M−Mo bimetallic catalysts (M = Co or Cu) supported on TiO_2 and employed them in the CDRM reaction process. They obtained good conversion rates at a temperature of 800°C, about 81% and 86% for CH_4 and CO_2, respectively, with a 0.9 H_2/CO ratio for the CoMo1 catalyst. On the other hand, the CuMo1 catalyst achieved 76% and 62% of CH_4 and CO_2 conversion rates respectively, with a 0.8 H_2/CO ratio of syngas (Nguyen et al.,

2020). Also, (Kim et al., 2015) synthesized bare Ni and TiO_2-coated Ni particles and employeed them in the CDRM reaction at 800 °C. The latter catalyst showed good catalytic activity with 55-60% CO_2 conversion rates. On the other hand TiO_2/Ni catalyst showed higher stability, catalytic activity, and H_2 selectivity with time, as compared with the bare Ni (Kim et al., 2015). Another study that applied TiO_2 as support material in their preparation was reported by (Xie et al., 2022), who synthesized a Ni supported on mesoporous TiO_2 photothermal catalyst and used it in the methane dry reforming reactions. They demonstrated a superior catalytic activity compared to other catalysts reported in the literature due to the high thermal stability of TiO_2 (Xie et al., 2022).

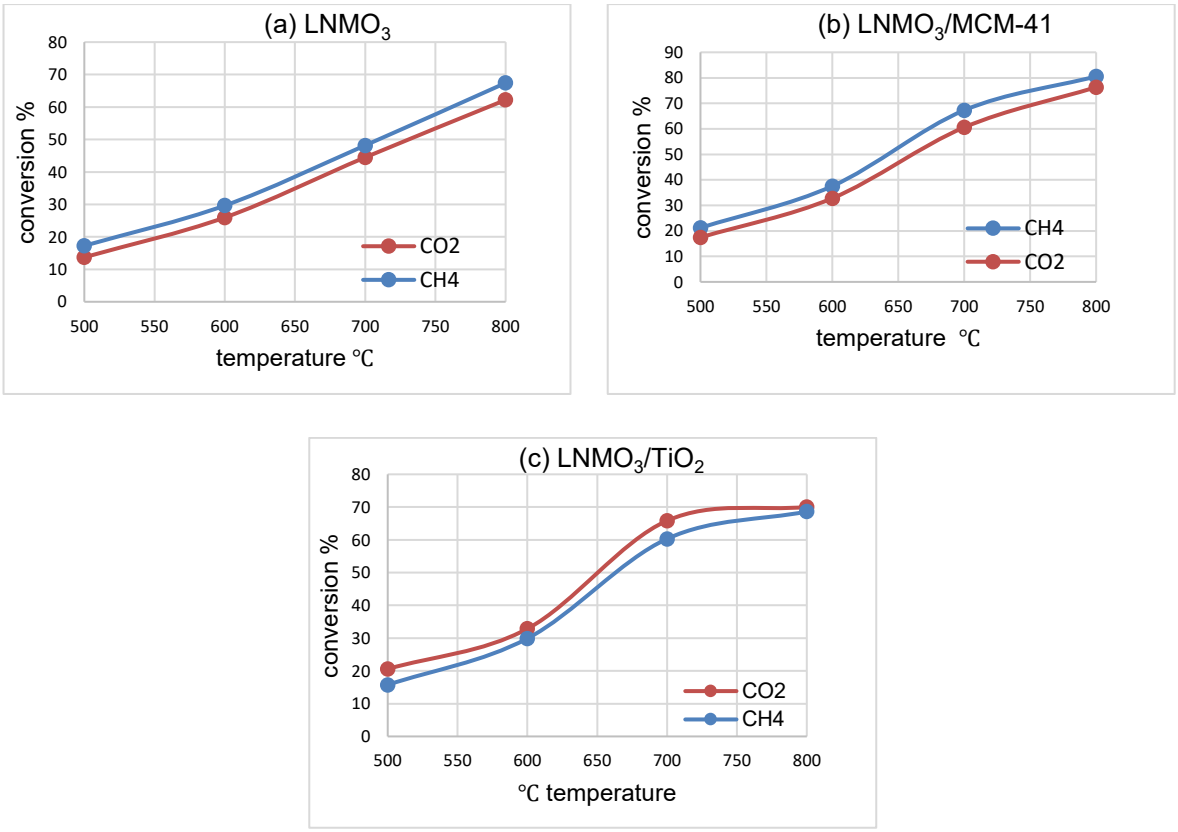

Fig. 10. (a) CH_4 and CO_2 conversions after 1 hr of reaction for the $LNMO_3$ sample, (b) for the $LNMO_3$/MCM-41 sample, (c) for $LNMO_3/TiO_2$.

3.1.8. Stability test

The stability of a catalyst is essential for its effectiveness and performance, especially in high-temperature reactions. A stable catalyst can overcome some challenges like carbon deposition and sintering at elevated temperatures, and it remains effective even in the situation of catalyst poisoning. Thus, the stability test for our prepared catalysts was conducted in the reactor with the conditions of a 1:1 molar feed ratio of CH_4:CO_2 at 800 °C for 15 hrs. Fig. 11a shows the change in CH_4 and CO_2 conversion rates with time using the $LNMO_3$ catalyst. Fig. 11a displays that during the first hour of the reaction, the conversion of CH_4 at 800 °C is 80.56%. Then, the

conversion decreases gradually until it reaches its lowest value of 68.04% after 15 hr of reaction. For CO_2, also through the first hour of reaction, the conversion is 76.32%; it slightly decreases to 63.19% after 15 hr of reaction.

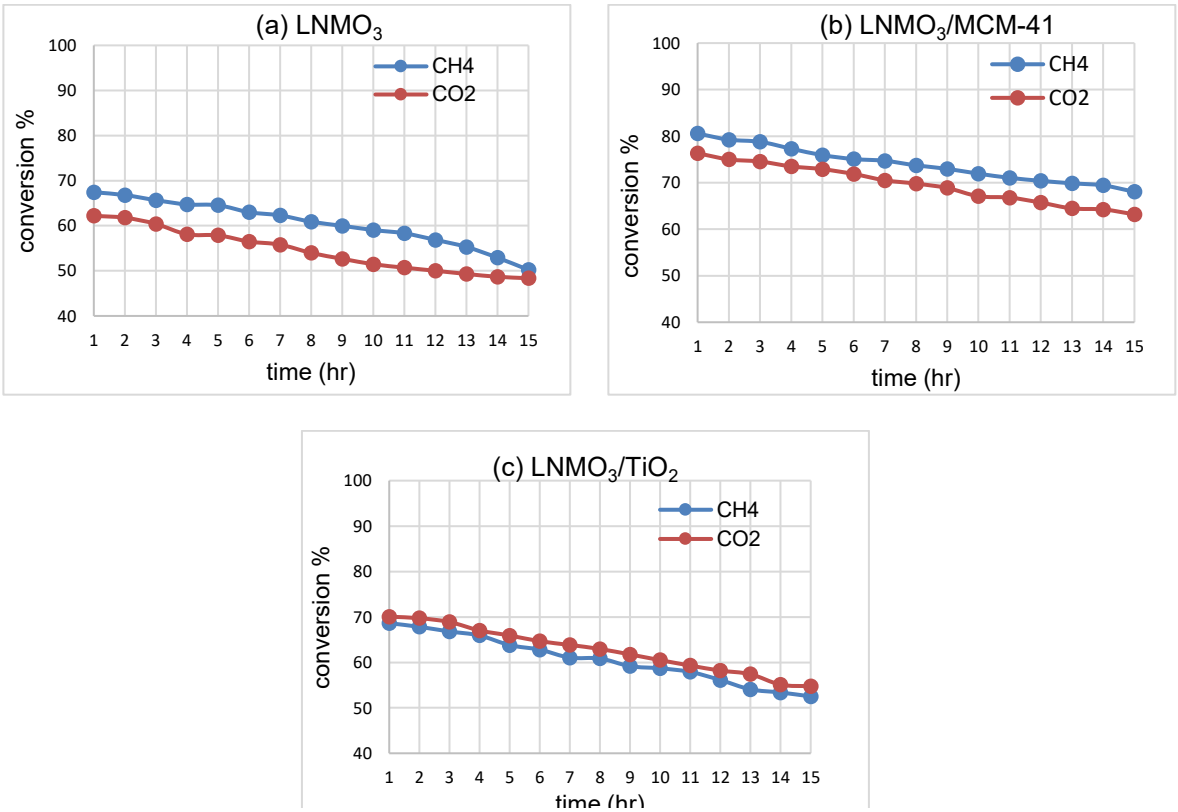

Fig. 11. Conversion changes of CH_4 and CO_2 versus time for (a) $LNMO_3$, (b) $LNMO_3$/MCM-41, (c) $LNMO_3/TiO_2$

At 800 °C, it is noticed that the $LNMO_3$/MCM-41 catalyst exhibited better catalytic stability in comparison to the other two catalysts in 15 hr of reaction, as shown in Fig. 11b. This improved performance is due to the high surface area of mesoporous MCM-41 support, making it effective as a support to improve the dispersion of Ni particles (Tian et al., 2009). The initial conversions for $LNMO_3$ of CH_4 and CO_2 gradually decrease with the increasing time of the reaction stream. This may be attributed to the formation of carbon deposits on the catalyst surface, causing a blockage in the pores of the active sites; consequently, fewer gas molecules can enter, and a decrease in activity occurs with time (Wang et al., 2013). Although the catalysts showed a continuous decrease in activity over time, they have good stability compared to other Ni-based catalysts used in the CDRM reaction. This is actually attributed to the existence of La metal since it has good catalytic properties due to its ability to enhance the redox reaction, enabling the catalyst to oxidize the hydrocarbons and CO_2, and it could accelerate the development of crucial precursors that react to produce syngas, as reported by (Akri et al., 2017). They prepared NiCe and NiLa catalysts, supported on natural illite clay for the reaction

of auto-thermal reforming of methane. They found that the presence of lanthanum improved the catalytic stability for 24 hours on the reaction stream at 800 °C. This can be related to the production of a britholite phase during the reaction caused by lanthanum migration into the bulk. This phase could hinder the growth of $FeNi_3$ alloy on Ce-based materials, which are less active than metallic Ni nanoparticles during dry reforming reactions (Akri et al., 2017). The good performance can also be attributed to the presence of MnO species as well as La_2O_3, (Kim et al., 2019).They made a study on $LaNi_{0.34}Co_{0.33}Mn_{0.33}O_3$ catalyst and investigated its activity in the CDRM reaction. The study proved high activity and stability results with low carbon formation due to the strong interactions between metals and La_2O_3 support, which was caused by MnO (Kim et al., 2019).

After the reduction process, a complete decomposition process for the perovskite phase was detected, forming Ni and La_2O_3 species. The produced Ni particles are evenly distributed on the La_2O_3 support. This distribution is defined by a strong metal-support interaction. Furthermore, the formation of $La_2O_2CO_3$ through $La_2O_3+CO_2 \rightarrow La_2O_2CO_3$ reaction process improves the activity of the lattice oxygen and assists the removal of carbon species adsorbed on the Ni surface by $La_2O_2CO_3$ formation (Kim et al., 2019). In comparison, (Liu et al., 2009) prepared 2Ni–1Mn, 2Ni–1Ti, and Ni–MCM-41 samples, compared to Ni–MCM–41, and they found that the catalytic activity and stability of 2Ni–1Mn and 2Ni–1Ti catalysts were significantly low. Since 2Ni–1Mn and 2Ni–1Ti catalysts suffered from deactivation, the high thermal stability of the MCM-41 structure is attributed to this enhanced stability (Liu et al., 2009).

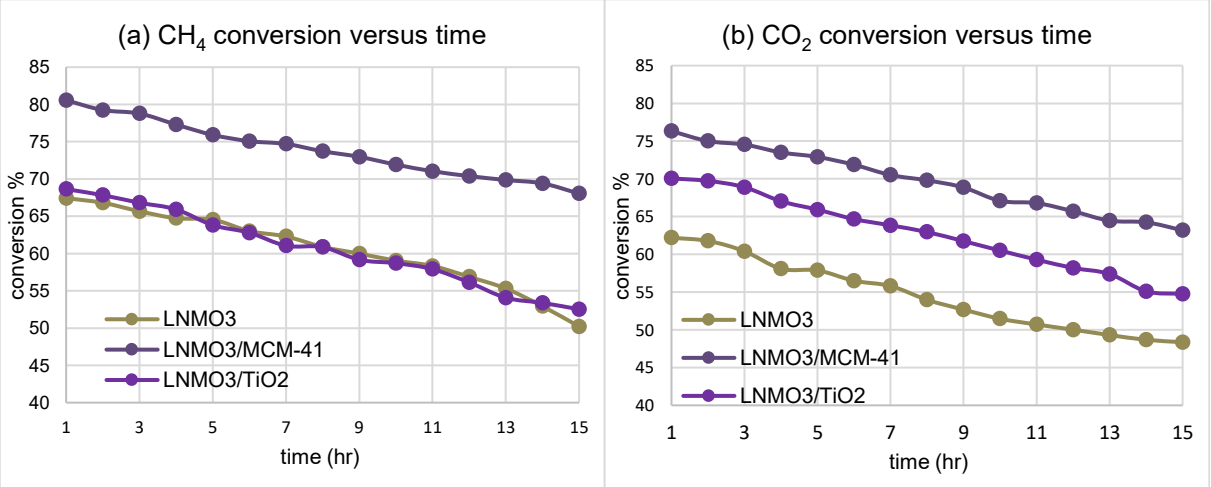

Fig. 12. (a) CH_4 conversion with time, (b): CO_2 conversion with time.

3.1.9. H_2/CO ratio

The selectivity of H_2/CO of the three prepared catalysts was estimated using Eq. (4.1)

$$\frac{H2}{CO} = (3 - \frac{r_{CO2}}{r_{CH4}})/(1 + \frac{r_{CO2}}{r_{CH4}}) \quad (4.1)$$

Figs. 13 (a, b, and c) show the H_2/CO ratio for $LNMO_3$, $LNMO_3$/MCM-41, and $LNMO_3/TiO_2$, respectively.

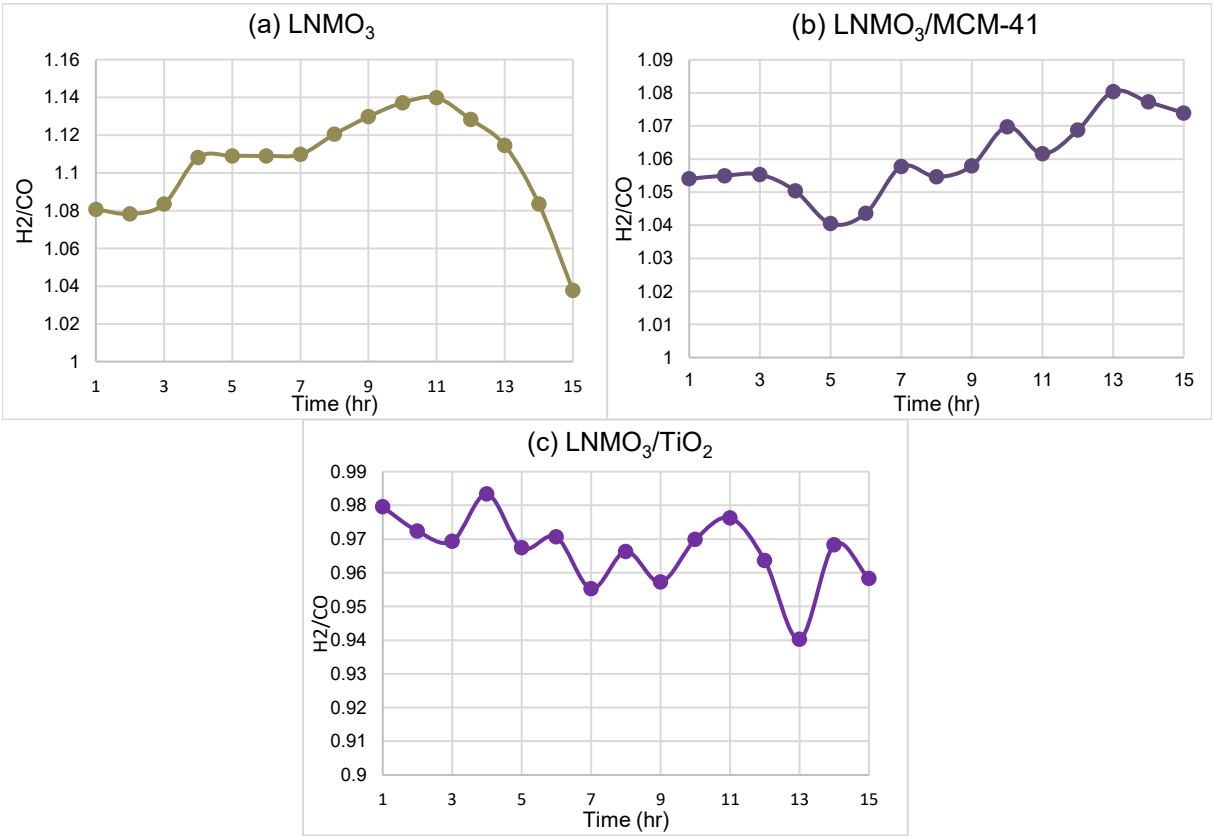

Fig. 13. H_2/CO ratio of CH_4 and CO_2 versus time for (a) $LNMO_3$, (b) $LNMO_3$/MCM-41, (c) $LNMO_3/TiO_2$

Fig. 13a shows the H_2/CO ratio of $LNMO_3$ through 15 hrs of reaction. We can observe that the values are greater than 1, and this result is attributed to the occurrence of Boudouard side reaction (Eq. (4.1)) $2CO \rightarrow C + CO_2$. This reaction consumes the product CO, consequently increasing the H_2 amount in the product gas; thus, the H_2/CO ratio is greater than 1 (Lanre et al., 2022). After adding MCM-41 support material, the H_2/CO ratio is also higher than 1 as shown in Fig. 13b, which means that the Boudouard side reaction is still happening. On the other hand, Fig. 13c indicates that the H_2/CO ratio of $LNMO_3/TiO_2$ is less than 1 due to the occurrence of reverse water gas shift reaction (RWGS) simultaneously parallel with the CDRM reaction Eq. (4.2) $CO_2 + H_2 \leftrightarrow H_2O + CO$. This reaction consumes the product, H_2, consequently increasing the CO amount in the product gas; thus, the H_2/CO ratio is less than 1

(Cargnello et al., 2013). Several researchers obtained similar results; for example, (Kim et al., 2019) prepared $LaNi_{0.34}Co_{0.33}Mn_{0.33}O_3$ catalyst and employed it in the CDRM reaction. The authors indicated that the H_2/CO ratio was greater than 1, and they explained this behavior due to the Boudouard side reaction ($2CO \rightarrow C+CO_2$), which agrees with our result (Kim et al., 2019). Another study obtained a H_2/CO ratio higher than 1 (Shahnazi and Firoozi, 2021) with their prepared perovskites catalysts $LaNi_{1-x}Mn_xO_3$ ($0<x<1$). The catalytic performance in the CDRM reaction was detected, which indicated the H_2/CO ratio for all samples was higher than 1. This results can be interpreted as a result of the occurrence of the Boudouard side reaction as well. Another study reported by (Hu et al., 2018) in their study they got a similar result to our study in which they used TiO_2 as a support when synthesizing Ni/TiO_2 catalyst. The catalytic performance in the CDRM reaction showed that the H_2/CO ratio was less than one due to the reverse water gas shift reaction (Hu et al., 2018).

4. CONCLUSIONS

$LaNiMnO_3$ ($LNMO_3$) and supported $LaNiMnO_3$ over MCM-41 and TiO_2 ($LNMO_3$/MCM-41 and $LNMO_3/TiO_2$) were successfully prepared via sol-gel preparation method. Important insights into the catalysts' structural, textural, and chemical properties were obtained by conducting a number of characterization techniques (BET, TGA, XRD, FE-SEM, EDS, and FTIR) to characterize the prepared samples. It was found that the incorporation of (MCM-41 and TiO_2) supports extensively influences the physicochemical properties and the catalytic performance of the $LNMO_3$ catalyst.

BET test showed that adding support materials increased the surface area and porosity of the catalysts. A higher surface area value was obtained with $LNMO_3$/MCM-41 and $LNMO_3/TiO_2$ than $LNMO_3$, about 156.4 m^2/g and 21.7 m^2/g, respectively, and the pore volume also increased to 1.532, and 0.020 cm^3/g, respectively. TGA results indicated that the thermal stability of the catalysts, with TiO_2 support, contributed to lower weight loss and, thus, lower carbon deposition than $LNMO_3$ and $LNMO_3$/MCM-41. The carbon deposition was in this order: $LNMO_3$/MCM-41> $LNMO_3$> $LNMO_3/TiO_2$, resulting in resistance to deactivation processes at high temperatures. Based on the XRD results, all catalysts showed a rhombohedral $LaNiO_3$ perovskite structure, La-Ni-Mn-O solid solution, La_2O_3, metallic nickel, and NiO compounds, and no impurity phases such as $NiMnO_3$ or $Ni_3Mn_2O_8$ were indicated, as well as the support addition enhanced the crystallite size and phase composition. Also, FE-SEM imaging shows that the morphologies were more regular for the supported catalysts than the unsupported ones, in which MCM-41 and TiO_2 showed a better dispersion for the active components, higher

surface area, and consequently better morphology. Catalytic activity and stability tests confirmed that the choice of selected supports significantly affected the efficiency of CDRM reactions. The support addition improved the $LNMO_3$ performance in terms of activity and stability within 15 hr of reaction. In which CH_4 and CO_2 conversion rates for the three catalysts were in this order: $LNMO_3$/MCM-41> $LNMO_3/TiO_2$> $LNMO_3$. The higher conversion rates with $LNMO_3$/MCM-41 were about 80.56% for CH_4 and 76.32% for CO_2. In terms of stability, they were in the same order. The catalysts showed good stability, whereas La metal helped obtain good stability performance due to its catalytic activity. Several side reactions occurred simultaneously with the CDRM reaction in which $LNMO_3$ and $LNMO_3$/MCM-41 exhibited a H_2/CO ratio higher than 1, owning to the occurrence of the Boudouard reaction. On the other hand, $LNMO_3/TiO_2$ exhibited a H_2/CO ratio of less than 1 due to the reverse water gas shift reaction (RWGS).

In summary, the current study underscores the critical influence of support materials on the performance of $LaNiMnO_3$ catalyst for the catalytic dry reforming of methane. The insights of this study pave the path for the development of more effective catalysts by carefully selecting and optimizing support materials to improve catalytic activity and stability in the CDRM processes.

ACKNOWLEDGEMENTS

The authors are grateful to the Chemical Engineering Department, College of Engineering, and the Oil and Gas Refining Department, College of Petroleum Process Engineering, Tikrit University, for granting access to their laboratories. We admire the work of the technical staff of the Petroleum Research and Development Center and Alkhora nano lab at Alkhora Company in Baghdad, Iraq. Also, thanks to Alfaisal Aljbory for his assistance.

SUBSCRIPTS

CDRM	Catalytic dry reforming of methane
$LNMO_3$	$LaNiMnO_3$
$LNMO_3$/MCM-41	$LaNiMnO_3$/MCM-41
$LNMO_3/TiO_2$	$LaNiMnO_3/TiO_2$

5. REFERENCES

ABDULRASHEED, A., JALIL, A. A., GAMBO, Y., IBRAHIM, M., HAMBALI, H. U. & HAMID, M. Y. S. 2019. A review on catalyst development for dry reforming of methane to syngas: Recent advances. Renewable and Sustainable Energy Reviews, 108, 175-193.

ABED, S. S., SEDIQHI, M. & DIWAN, A. 2023. INFLUENCE OF AL2O3 NANO ADDITIVES ON THE VISCOSITY AND THERMAL CONDUCTIVITY OF DOUBLE DISTILLED WATER. Kufa Journal of Engineering, 14, 12-23.

AKRI, M., PRONIER, S., CHAFIK, T., ACHAK, O., GRANGER, P., SIMON, P., TRENTESAUX, M. & BATIOT-DUPEYRAT, C. 2017. Development of nickel supported La and Ce-natural illite clay for autothermal dry reforming of methane: Toward a better resistance to deactivation. Applied Catalysis B: Environmental, 205, 519-531.

ALAHMAD, S. 2012. Modification of mesoporous silica MCM-41 and its applications-A review. Oriental Journal of Chemistry, 28, 1.

ALI, A. A., MOHAMMED, H. & AHMED, S. 2024. A Comprehensive Review of the Impact of CO2 Emissions on Global Warming and the Potential Using Solar Energy Mitigation. Al-Rafidain Journal of Engineering Sciences, 319-340.

AMIN, M. H., TARDIO, J. & BHARGAVA, S. K. 2013. A comparison study on carbon dioxide reforming of methane over Ni catalysts supported on mesoporous SBA-15, MCM-41, KIT-6 and gamma-Al2. Chemeca 2013 (41st: 2013: Brisbane, Qld.). Chemeca 2013: Challenging Tomorrow. Barton, ACT: Engineers Australia, 543-548.

BAAMRAN, K. S. & TAHIR, M. 2019. Ni-embedded TiO2-ZnTiO3 reducible perovskite composite with synergistic effect of metal/support towards enhanced H2 production via phenol steam reforming. Energy Conversion and Management, 200, 112064.

BAHRUJI, H., BOWKER, M., DAVIES, P. R., AL-MAZROAI, L. S., DICKINSON, A., GREAVES, J., JAMES, D., MILLARD, L. & PEDRONO, F. 2010. Sustainable H2 gas production by photocatalysis. Journal of Photochemistry and Photobiology A: Chemistry, 216, 115-118.

BATIOT-DUPEYRAT, C., GALLEGO, G. A. S., MONDRAGON, F., BARRAULT, J. & TATIBOUËT, J.-M. 2005. CO2 reforming of methane over LaNiO3 as precursor material. Catalysis Today, 107, 474-480.

BHATTACHARYYA, S., LELONG, G. & SABOUNGI, M.-L. 2006. Recent progress in the synthesis and selected applications of MCM-41: a short review. Journal of Experimental Nanoscience, 1, 375-395.

BHAVANI, A. & LEE, J. 2018. Autothermal CO2 Reforming with Methane Over Crystalline LaMn1-XNiXO3 Perovskite Catalysts. Int J Metall Met Phys, 3, 1-6.

BHAVANI, A. G., KIM, W. Y. & LEE, J. S. 2013. Barium substituted lanthanum manganite perovskite for CO2 reforming of methane. ACS Catalysis, 3, 1537-1544.

BIAN, Z., WANG, Z., JIANG, B., HONGMANOROM, P., ZHONG, W. & KAWI, S. 2020. A review on perovskite catalysts for reforming of methane to hydrogen production. Renewable and Sustainable Energy Reviews, 134, 110291.

BLASCO, J., SANCHEZ, M. C., PEREZ-CACHO, J., GARCıA, J., SUBıAS, G. & CAMPO, J. 2002. Synthesis and structural study of LaNi1- xMnxO3+ δ perovskites. Journal of Physics and Chemistry of Solids, 63, 781-792.

CAO, Y., LI, H., ZHANG, J., SHI, L. & ZHANG, D. 2016. Promotional effects of rare earth elements (Sc, Y, Ce, and Pr) on NiMgAl catalysts for dry reforming of methane. RSC advances, 6, 112215-112225.

CARGNELLO, M., DOAN-NGUYEN, V. V., GORDON, T. R., DIAZ, R. E., STACH, E. A., GORTE, R. J., FORNASIERO, P. & MURRAY, C. B. 2013. Control of metal nanocrystal size reveals metal-support interface role for ceria catalysts. Science, 341, 771-773.

CHAI, Y., FU, Y., FENG, H., KONG, W., YUAN, C., PAN, B., ZHANG, J. & SUN, Y. 2018. A Nickel-Based Perovskite Catalyst with a Bimodal Size Distribution of Nickel Particles for Dry Reforming of Methane. ChemCatChem, 10, 2078-2086.

CHEN, C., ZHOU, J., GENG, J., BAO, R., WANG, Z., XIA, J. & LI, H. 2020. Perovskite LaNiO3/TiO2 step-scheme heterojunction with enhanced photocatalytic activity. Applied Surface Science, 503, 144287.

DA SILVA, P. R. N. & ZANOTELI, K. 2020. Evaluation of Nickel Catalysts Supported in Dry Methane Reform Aiming at Hydrogen Production/Case of Supports: SiO2, La2O3 MCM-41, and Al2O3. Orbital: The Electronic Journal of Chemistry, 140-147.

DAZA, C. E., GALLEGO, J., MORENO, J. A., MONDRAGÓN, F., MORENO, S. & MOLINA, R. 2008. CO2 reforming of methane over Ni/Mg/Al/Ce mixed oxides. Catalysis Today, 133, 357-366.

DE ARAUJO, G. C., DE LIMA, S. M., ASSAF, J. M., PEÑA, M. A., FIERRO, J. L. G. & DO CARMO RANGEL, M. 2008. Catalytic evaluation of perovskite-type oxide LaNi1- xRuxO3 in methane dry reforming. Catalysis Today, 133, 129-135.

DEHGHANGHADIKOLAEI, A., ANSARY, J. & GHOREISHI, R. 2018. Sol-gel process applications: A mini-review. Proc. Nat. Res. Soc, 2, 02008-02029.

DEKKAR, S., TEZKRATT, S., SELLAM, D., IKKOUR, K., PARKHOMENKO, K., MARTINEZ-MARTIN, A. & ROGER, A. C. 2020. Dry Reforming of Methane over Ni–Al2O3 and Ni–SiO2 Catalysts: Role of Preparation Methods. Catalysis Letters, 150, 2180-2199.

DINAMARCA, R., SEPÚLVEDA, C., DELGADO, E. J., PEÑA, O., FIERRO, J. L. G. & PECCHI, G. 2016. Electronic properties and catalytic performance for DME combustion of lanthanum manganites with partial B-site substitution. Journal of Catalysis, 338, 47-55.

DUAN, Q., WANG, J., DING, C., DING, H., GUO, S., JIA, Y., LIU, P. & ZHANG, K. 2017. Partial oxidation of methane over Ni based catalyst derived from order mesoporous LaNiO3 perovskite prepared by modified nanocasting method. Fuel, 193, 112-118.

FARHADI, S. & MAHMOUDI, F. 2019. Improving the adsorption ability of perovskite-type LaNiO3 nanomaterial towards organic dyes by hybridizing with phosphotungstic acid. Polyhedron, 169, 39-50.

FRONTERA, P., MACARIO, A., ALOISE, A., ANTONUCCI, P. L., GIORDANO, G. & NAGY, J. B. 2013. Effect of support surface on methane dry-reforming catalyst preparation. Catalysis today, 218, 18-29.

GALLEGO, G. S., MARÍN, J. G., BATIOT-DUPEYRAT, C., BARRAULT, J. & MONDRAGÓN, F. 2009. Influence of Pr and Ce in dry methane reforming catalysts produced from La1- xAxNiO3- δ perovskites. Applied Catalysis A: General, 369, 97-103.

GALLEGO, G. S., MONDRAGÓN, F., BARRAULT, J., TATIBOUËT, J.-M. & BATIOT-DUPEYRAT, C. 2006. CO2 reforming of CH4 over La–Ni based perovskite precursors. Applied Catalysis A: General, 311, 164-171.

GIROIR-FENDLER, A., ALVES-FORTUNATO, M., RICHARD, M., WANG, C., DÍAZ, J. A., GIL, S., ZHANG, C., CAN, F., BION, N. & GUO, Y. 2016. Synthesis of oxide supported LaMnO3 perovskites to enhance yields in toluene combustion. Applied Catalysis B: Environmental, 180, 29-37.

GOLDWASSER, M. R., RIVAS, M. E., PIETRI, E., PÉREZ-ZURITA, M. J., CUBEIRO, M. L., GRIVOBAL-CONSTANT, A. & LECLERCQ, G. 2005. Perovskites as catalysts precursors: synthesis and characterization. Journal of Molecular Catalysis A: Chemical, 228, 325-331.

HAMBALI, H. U., JALIL, A. A., ABDULRASHEED, A. A., SIANG, T. J., ABDULLAH, T. A. T., AHMAD, A. & VO, D. V. N. 2020. Fibrous spherical Ni-M/ZSM-5 (M: Mg, Ca, Ta, Ga)

catalysts for methane dry reforming: The interplay between surface acidity-basicity and coking resistance. International Journal of Energy Research, 44, 5696-5712.

HAN, Y., WEN, B., ZHU, M. & DAI, B. 2018. Lanthanum incorporated in MCM-41 and its application as a support for a stable Ni-based methanation catalyst. Journal of Rare Earths, 36, 367-373.

HAYAL, A. L., AL-GHARRAWI, A. M. & FATTAH, M. Y. 2021. Effect of nanomaterials on shear strength of gypseous soil. Kufa Journal of Engineering, 12, 1-14.

HOU, Y.-C., DING, M.-W., LIU, S.-K., WU, S.-K. & LIN, Y.-C. 2014. Ni-substituted LaMnO 3 perovskites for ethanol oxidation. RSC advances, 4, 5329-5338.

HU, D., LIU, C., LI, L., LV, K.-L., ZHANG, Y.-H. & LI, J.-L. 2018. Carbon dioxide reforming of methane over nickel catalysts supported on TiO2 (001) nanosheets. international journal of hydrogen energy, 43, 21345-21354.

IBRAHIM, A. A., FAKEEHA, A. H., AL-FATESH, A. S., ABASAEED, A. E. & KHAN, W. U. 2015. Methane decomposition over iron catalyst for hydrogen production. International Journal of Hydrogen Energy, 40, 7593-7600.

ISHAQ, H. & DINCER, I. 2021. Comparative assessment of renewable energy-based hydrogen production methods. Renewable and Sustainable Energy Reviews, 135, 110192.

JANG, W.-J., SHIM, J.-O., KIM, H.-M., YOO, S.-Y. & ROH, H.-S. 2019. A review on dry reforming of methane in aspect of catalytic properties. Catalysis Today, 324, 15-26.

JOHANSSON, T., PAKHARE, D., HAYNES, D., ABDELSAYED, V., SHEKHAWAT, D. & SPIVEY, J. 2014. Characterization of LaRhO3 perovskites for dry (CO2) reforming of methane (DRM). Chemical Papers, 68.

KHALESI, A., ARANDIYAN, H. R. & PARVARI, M. 2008. Effects of lanthanum substitution by strontium and calcium in La-Ni-Al perovskite oxides in dry reforming of methane. Chinese Journal of Catalysis, 29, 960-968.

KIM, D. H., KIM, S. Y., HAN, S. W., CHO, Y. K., JEONG, M.-G., PARK, E. J. & KIM, Y. D. 2015. The catalytic stability of TiO2-shell/Ni-core catalysts for CO2 reforming of CH4. Applied Catalysis A: General, 495, 184-191.

KIM, S. S., CHOI, H. J. & HONG, S. C. 2012. Effect of pretreatment time in dry reforming over Ni/TiO2 catalyst. Journal of chemical engineering of Japan, 45, 41-45.

KIM, W. Y., JANG, J. S., RA, E. C., KIM, K. Y., KIM, E. H. & LEE, J. S. 2019. Reduced perovskite LaNiO3 catalysts modified with Co and Mn for low coke formation in dry reforming of methane. Applied Catalysis A: General, 575, 198-203.

KIM, Y. T., LEE, J.-J. & LEE, J. 2023. Electricity-driven reactors that promote thermochemical catalytic reactions via joule and induction heating: a review. Chemical Engineering Journal, 144333.

KIRA, H., TAMURA, H., ANDO, Y., ONODERA, M., NAKAO, H., MURAKAMI, Y., TSUDA, K., OHOYAMA, K., YAMAZAKI, S. & TAJIRI, T. 2007. Magnetic properties of LaMnO3+ δ nanocrystals in MCM-41 mesoporous silica. Journal of magnetism and magnetic materials, 310, 2480-2482.

KOMARALA, E. P., KOMISSAROV, I. & ROSEN, B. A. 2019. Effect of Fe and Mn substitution in LaNiO3 on exsolution, activity, and stability for methane dry reforming. Catalysts, 10, 27.

LANRE, M. S., ABASAEED, A. E., FAKEEHA, A. H., IBRAHIM, A. A., ALQURAINI, A. A., ALRESHAIDAN, S. B. & AL-FATESH, A. S. 2022. Modification of CeNi0. 9Zr0. 1O3 perovskite catalyst by partially substituting yttrium with zirconia in dry reforming of methane. Materials, 15, 3564.

LI, L., CHEN, J., ZHANG, Q., YANG, Z., SUN, Y. & ZOU, G. 2020. Methane dry reforming over activated carbon supported Ni-catalysts prepared by solid phase synthesis. Journal of Cleaner Production, 274, 122256.

LI, M., SUN, Z. & HU, Y. H. 2021. Catalysts for CO 2 reforming of CH 4: A review. Journal of Materials Chemistry A, 9, 12495-12520.

LI, Z. J., HOFMAN, E., LI, J., DAVIS, A. H., TUNG, C. H., WU, L. Z. & ZHENG, W. 2018. Photoelectrochemically active and environmentally stable CsPbBr3/TiO2 core/shell nanocrystals. Advanced Functional Materials, 28, 1704288.

LIU, C., CHEN, D., CAO, Y., MAO, Y., WANG, W., WANG, Z. & KAWI, S. 2020. Catalytic steam reforming of in-situ tar from rice husk over MCM-41 supported LaNiO3 to produce hydrogen rich syngas. Renewable Energy, 161, 408-418.

LIU, D., QUEK, X. Y., CHEO, W. N. E., LAU, R., BORGNA, A. & YANG, Y. 2009. MCM-41 supported nickel-based bimetallic catalysts with superior stability during carbon dioxide

reforming of methane: Effect of strong metal–support interaction. Journal of Catalysis, 266, 380-390.

LIU, F., QU, Y., YUE, Y., LIU, G. & LIU, Y. 2015. Nano bimetallic alloy of Ni–Co obtained from LaCo x Ni 1- x O 3 and its catalytic performance for steam reforming of ethanol. Rsc Advances, 5, 16837-16846.

MA, X., AI, C., CAO, J., LI, J., ZHU, Y. & JING, D. 2021. Heterojunction formed by TiO2 supported on lamellar La2NiO4 perovskite for enhanced visible-light-driven photocatalytic hydrogen production. Journal of Photonics for Energy, 11, 034001-034001.

MAKSHINA, E. V., SIROTIN, S. V., VAN DEN BERG, M. W. E., KLEMENTIEV, K. V., YUSHCHENKO, V. V., MAZO, G. N., GRÜNERT, W. & ROMANOVSKY, B. V. 2006. Characterization and catalytic properties of nanosized cobaltate particles prepared by in situ synthesis inside mesoporous molecular sieves. Applied Catalysis A: General, 312, 59-66.

MARIDEVARU, M. C., WU, J. J., VISWANATHAN MANGALARAJA, R. & ANANDAN, S. 2020. Ultrasonic-Assisted Preparation Of Perovskite-Type Lanthanum Nickelate Nanostructures and Its Photocatalytic Properties. ChemistrySelect, 5, 7947-7958.

MESSAOUDI, H., THOMAS, S., DJAIDJA, A., SLYEMI, S. & BARAMA, A. 2018. Study of LaxNiOy and LaxNiOy/MgAl2O4 catalysts in dry reforming of methane. Journal of CO2 Utilization, 24, 40-49.

MORADI, G., HEMMATI, H. & RAHMANZADEH, M. 2013. Preparation of a LaNiO ₃ /γ-Al ₂ O ₃ Catalyst and its Performance in Dry Reforming of Methane. Chemical Engineering & Technology, 36, 575-580.

MORADI, G. R. & RAHMANZADEH, M. 2012. The influence of partial substitution of alkaline earth with La in the LaNiO3 perovskite catalyst. Catalysis Communications, 26, 169-172.

MULEWA, W., TAHIR, M. & AMIN, N. A. S. 2017. MMT-supported Ni/TiO2 nanocomposite for low temperature ethanol steam reforming toward hydrogen production. Chemical Engineering Journal, 326, 956-969.

NAVAS, D., FUENTES, S., CASTRO-ALVAREZ, A. & CHAVEZ-ANGEL, E. 2021. Review on sol-gel synthesis of perovskite and oxide nanomaterials. Gels, 7, 275.

NGUYEN, H. M., PHAM, G. H., TADE, M., PHAN, C., VAGNONI, R. & LIU, S. 2020. Microwave-Assisted Dry and Bi-reforming of Methane over M–Mo/TiO ₂ (M = Co, Cu) Bimetallic Catalysts. Energy & Fuels, 34, 7284-7294.

NGUYEN, S. V., SZABO, V., ON, D. T. & KALIAGUINE, S. 2002. Mesoporous silica supported LaCoO3 perovskites as catalysts for methane oxidation. Microporous and Mesoporous Materials, 54, 51-61.

NISA, K. S., SUENDO, V., SOPHIANA, I. C., SUSANTO, H., KUSUMAATMAJA, A., NISHIYAMA, N. & BUDHI, Y. W. 2022. Effect of base promoter on activity of MCM-41-supported nickel catalyst for hydrogen production via dry reforming of methane. International Journal of Hydrogen Energy, 47, 23201-23212.

NUVULA, S., SAGAR, T. V., VALLURI, D. K. & PRASAD, P. S. S. 2018. Selective substitution of Ni by Ti in LaNiO3 perovskites: A parameter governing the oxy-carbon dioxide reforming of methane. International Journal of Hydrogen Energy, 43, 4136-4142.

OMARI, E., MAKHLOUFI, S. & OMARI, M. 2017. Preparation by sol–gel method and characterization of Co-doped LaNiO 3 perovskite. Journal of Inorganic and Organometallic Polymers and Materials, 27, 1466-1472.

ÖZBAY, N. & ŞAHIN, R. Z. Preparation and characterization of LaMnO3 and LaNiO3 perovskite type oxides by the hydrothermal synthesis method. 2017 2017. AIP Publishing.

PEREÑIGUEZ, R., GONZALEZ-DELACRUZ, V. M., CABALLERO, A. & HOLGADO, J. P. 2012. LaNiO3 as a precursor of Ni/La2O3 for CO2 reforming of CH4: Effect of the presence of an amorphous NiO phase. Applied Catalysis B: Environmental, 123, 324-332.

RABELO-NETO, R. C., SALES, H. B. E., INOCÊNCIO, C. V. M., VARGA, E., OSZKO, A., ERDOHELYI, A., NORONHA, F. B. & MATTOS, L. V. 2018. CO2 reforming of methane over supported LaNiO3 perovskite-type oxides. Applied Catalysis B: Environmental, 221, 349-361.

RAHMAN, F. A., AZIZ, M. M. A., SAIDUR, R., BAKAR, W. A. W. A., HAININ, M. R., PUTRAJAYA, R. & HASSAN, N. A. 2017. Pollution to solution: Capture and sequestration of carbon dioxide (CO2) and its utilization as a renewable energy source for a sustainable future. Renewable and Sustainable Energy Reviews, 71, 112-126.

RASE, H. F. 2013. Fixed-bed reactor design and diagnostics: gas-phase reactions, Butterworth-Heinemann.

SAGAR, T. V., SREELATHA, N., HANMANT, G., SURENDAR, M., LINGAIAH, N., RAO, K. S. R., SATYANARAYANA, C. V. V., REDDY, I. A. K. & PRASAD, P. S. S. 2014. Influence of method of preparation on the activity of La–Ni–Ce mixed oxide catalysts for dry reforming of methane. Rsc Advances, 4, 50226-50232.

SELLAM, D., IKKOUR, K., DEKKAR, S., MESSAOUDI, H., BELAID, T. & ROGER, A.-C. 2019. CO2 reforming of methane over LaNiO3 perovskite supported catalysts: influence of silica support. Bulletin of Chemical Reaction Engineering & Catalysis, 14, 568-578.

SHAHNAZI, A. & FIROOZI, S. 2021. Improving the catalytic performance of LaNiO3 perovskite by manganese substitution via ultrasonic spray pyrolysis for dry reforming of methane. Journal of CO2 Utilization, 45, 101455.

SHARMA, G., KUMAR, A., NAUSHAD, M., SHARMA, S., GHFAR, A. A., AHAMAD, T., SI, C. & STADLER, F. J. 2019. Graphene oxide supported La/Co/Ni trimetallic nano-scale systems for photocatalytic remediation of 2-chlorophenol. Journal of Molecular Liquids, 294, 111605.

SINGH, S., OMOREGBE, O., SIANG, T. J., FAYAZ, F. & VO, D.-V. N. A short review on mesoporous silica-supported catalysts for methane dry reforming.

SOCRATES, G. 2004. Infrared and Raman characteristic group frequencies: tables and charts, John Wiley & Sons.

SUN, G., YANG, Y., YAO, Z., SHI, Y. & MAO, W. 2021. Investigation on the key factors of MoP catalysts prepared by a carbothermal reduction method for dry reforming of methane. Catalysis Science & Technology, 11, 3818-3825.

THIERS, L., LEITENBERGER, B. J., MUKASYAN, A. S. & VARMA, A. 2000. Influence of preheating rate on kinetics of high-temperature gas–solid reactions. AIChE journal, 46, 2518-2524.

TIAN, L., ZHAO, X. H., LIU, B. S. & ZHANG, W. D. 2009. Preparation of an Industrial Ni-Based Catalyst and Investigation on CH ₄ /CO ₂ Reforming to Syngas. Energy & Fuels, 23, 607-612.

TOUAHRA, F., RABAHI, A., CHEBOUT, R., BOUDJEMAA, A., LERARI, D., SEHAILIA, M., HALLICHE, D. & BACHARI, K. 2016. Enhanced catalytic behaviour of surface dispersed nickel on LaCuO3 perovskite in the production of syngas: an expedient approach to carbon

resistance during CO2 reforming of methane. International journal of hydrogen energy, 41, 2477-2486.

USMAN, M., DAUD, W. M. A. W. & ABBAS, H. F. 2015. Dry reforming of methane: Influence of process parameters—A review. Renewable and Sustainable Energy Reviews, 45, 710-744.

VALDERRAMA, G., KIENNEMANN, A., DE NAVARRO, C. U. & GOLDWASSER, M. R. 2018. LaNi1-xMnxO3 perovskite-type oxides as catalysts precursors for dry reforming of methane. Applied Catalysis A: General, 565, 26-33.

VAZ, T. & SALKER, A. V. 2007. Preparation, characterization and catalytic CO oxidation studies on LaNi1- xCoxO3 system. Materials Science and Engineering: B, 143, 81-84.

WANG, N., YU, X., WANG, Y., CHU, W. & LIU, M. 2013. A comparison study on methane dry reforming with carbon dioxide over LaNiO3 perovskite catalysts supported on mesoporous SBA-15, MCM-41 and silica carrier. Catalysis today, 212, 98-107.

XIE, T., ZHANG, Z.-Y., ZHENG, H.-Y., XU, K.-D., HU, Z. & LEI, Y. 2022. Enhanced photothermal catalytic performance of dry reforming of methane over Ni/mesoporous TiO2 composite catalyst. Chemical Engineering Journal, 429, 132507.

XU, J., YANG, Y., LIU, B., KONG, Y., BOYU, D., GUO, Y., ZHOU, J.-H. & WANG, X. Ultrasound-Assisted Degradation of Lignin by Mcm-41-Based Perovskite. Available at SSRN 4065244.

XU, L., LIU, W., ZHANG, X., TAO, L., XIA, L., XU, X., SONG, J., ZHOU, W., FANG, X. & WANG, X. 2019. Ni/La ₂ O ₃ Catalysts for Dry Reforming of Methane: Insights into the Factors Improving the Catalytic Performance. ChemCatChem, 11, 2887-2899.

YADAV, P. K. & DAS, T. 2019. Production of syngas from carbon dioxide reforming of methane by using LaNixFe1- xO3 perovskite type catalysts. International Journal of Hydrogen Energy, 44, 1659-1670.

YANG, E.-H., KIM, N. Y., NOH, Y.-S., LIM, S. S., JUNG, J.-S., LEE, J. S., HONG, G. H. & MOON, D. J. 2015. Steam CO2 reforming of methane over La1− xCexNiO3 perovskite catalysts. International Journal of Hydrogen Energy, 40, 11831-11839.

YANG, E.-H. & MOON, D. J. 2016. Synthesis of LaNiO 3 perovskite using an EDTA-cellulose method and comparison with the conventional Pechini method: application to steam CO 2 reforming of methane. RSC advances, 6, 112885-112898.

ZHANG, C., ZENG, K., WANG, C., LIU, X., WU, G., WANG, Z. & WANG, D. 2020. LaMnO3 perovskites via a facile nickel substitution strategy for boosting propane combustion performance. Ceramics International, 46, 6652-6662.

ZHANG, L., WANG, X., CHEN, C., ZOU, X., DING, W. & LU, X. 2017. Dry reforming of methane to syngas over lanthanum-modified mesoporous nickel aluminate/γ-alumina nanocomposites by one-pot synthesis. International Journal of Hydrogen Energy, 42, 11333-11345.

ZHANG, R., YANG, W., LUO, N., LI, P., LEI, Z. & CHEN, B. 2014. Low-temperature NH3-SCR of NO by lanthanum manganite perovskites: Effect of A-/B-site substitution and TiO2/CeO2 support. Applied catalysis B: environmental, 146, 94-104.

ZHANG, T. & LIU, Q. 2020. Mesostructured cellular foam silica supported bimetallic LaNi1-xCoxO3 catalyst for CO2 methanation. International Journal of Hydrogen Energy, 45, 4417-4426.

ZHAO, L., HAN, T., WANG, H., ZHANG, L. & LIU, Y. 2016. Ni-Co alloy catalyst from LaNi1− xCoxO3 perovskite supported on zirconia for steam reforming of ethanol. Applied Catalysis B: Environmental, 187, 19-29.

ZHENG, J., LIU, J., ZHAO, Z., XU, J., DUAN, A. & JIANG, G. 2012. The synthesis and catalytic performances of three-dimensionally ordered macroporous perovskite-type LaMn1-xFexO3 complex oxide catalysts with different pore diameters for diesel soot combustion. Catalysis Today, 191, 146-153.

ZHU, Y., SUN, Y., NIU, X., YUAN, F. & FU, H. 2010. Preparation of La-Mn-O perovskite catalyst by microwave irradiation method and its application to methane combustion. Catalysis letters, 135, 152-158.